STATE OF THE CLIMATE IN 2011

Special Supplement to the
Bulletin of the American Meteorological Society
Vol. 93, No. 7, July 2012

STATE OF THE CLIMATE IN 2011

Editors

Jessica Blunden

Derek S. Arndt

Associate Editors

Howard J. Diamond

A. Johannes Dolman

Ryan L. Fogt

Margarita C. Gregg

Bradley D. Hall

Martin O. Jeffries

Michele L. Newlin

James A. Renwick

Jacqueline A. Richter-Menge

Ahira Sánchez-Lugo

Ted A. Scambos

Wassila M. Thiaw

Peter W. Thorne

Scott J. Weaver

Kate M. Willett

AMERICAN METEOROLOGICAL SOCIETY

3. GLOBAL OCEANS—M. C. Gregg and M. L. Newlin, Eds.

a. Overview—M. C. Gregg and M. L. Newlin

The state of the oceans during 2011 was dominated by a moderate-to-strong La Niña during winter 2010/11 in the Pacific Ocean, followed by a return to near-normal conditions until the reemergence of another La Niña in August 2011. A strengthening of a negative Pacific decadal oscillation (PDO) also followed in the second half of 2011, with the development of a positive Indian Ocean dipole in the fall, and above-normal sea surface temperatures (SST) in the tropical North Atlantic and midlatitude southern oceans (section 3b). The global SST cooled by 0.1°C from 2010 to 2011 and changed from the 5th to 12th highest year since 1982, being associated with cooling influences of the 2010–12 La Niña (section 3b). However, the 2011 global integrals of upper ocean heat content are higher than for all prior years analyzed (section 3c). Overall in 2011, saltier (higher evaporation) regions of the ocean surface continued to be anomalously salty, and fresher (higher precipitation) regions anomalously fresh. This pattern, which has held since at least 2004, suggests an increase in the hydrological cycle, consistent with climate model predictions for a warming atmosphere (section 3e). These surface-forced changes extend to subsurface levels (section 3f) where long-term freshening in the water column of high latitudes in the Pacific Ocean is observed. A general year-to-year freshening was also seen in 2011 across much of the Atlantic, as well as in the Indian Ocean.

Relative to the long-term trend, global sea level dropped noticeably in mid-2010 and reached a local minimum in 2011. The drop was linked to the strong La Niña conditions throughout the latter part of 2010 and most of 2011. This sea level drop was followed by a sharp increase in global sea level during the second half of 2011 (section 3i). High values of chlorophyll were observed throughout much of the tropical Pacific Ocean, subtropical North Atlantic Ocean, tropical Indian Ocean, and in portions of the Southern Ocean. Conspicuously low values of chlorophyll were found in the western Indian Ocean, the tropical Atlantic, and globally throughout the subtropics (section 3j). The global net ocean CO_2 uptake for the 2010 transition period from El Niño to La Niña is estimated to be 1.30 Pg C yr^{-1} (PG = 10^{15} g), lower than the 29-year long-term mean of 1.47 Pg C yr^{-1} (section 3j). The 2010 global ocean inventory of anthropogenic CO_2 is 160 ± 26 Pg C (estimated using a Green's function method). The ocean inventory represents ~43% and ~29% of fossil fuel and total (fossil fuel and land use changes) anthropogenic CO_2 emissions, respectively, over the industrial period.

On a basin scale, the Pacific Ocean was dominated by both a negative Pacific decadal oscillation and two La Niña events (winter and fall). This resulted in below-normal 2011 sea surface temperatures in the tropical Pacific (coolest since 1985; section 3b). Zonal surface current anomalies in the tropical Pacific basin switched from negative values in late 2010 to El Niño-like (positive) values in early 2011, as SST anomalies reached their peak negative value. For the next months, as the surface current anomaly remained positive, the SST anomaly decreased in magnitude (section 3g). In the latter half of 2011, the surface current anomaly returned to neutral-to-La Niña-like (negative) values, leading the return of cold SST anomalies by several months. The warming trend in the western tropical Pacific and the cooling trend in the eastern tropical Pacific from 1993 to 2011 are consistent with a general trade wind intensification during that time period.

The Indian Ocean was influenced by a positive Indian Ocean dipole. The sea surface became fresher in 2011 relative to 2010 in the eastern equatorial Indian Ocean and the western equatorial Pacific, likely owing to La Niña, but saltier in the western tropical Pacific near 5°S, likely owing to a southward shift in the South Pacific convergence zone (section 3e). Overall, the tropical Indian Ocean cooled by 0.24°C from a historical high in 2010.

The Atlantic Ocean is characterized by the remote influence from the previous year El Niño, a persistent negative North Atlantic Oscillation (NAO), and a long-term cooling trend. The ocean net heat flux (i.e., the sum of shortwave radiation, longwave radiation, turbulent latent and sensible heat flux) anomalies showed a tripole structure in the North Atlantic associated with the change of NAO from a negative phase in 2010 to a more positive phase in 2011, and the fluxes were a forcing for SST variability (section 3d). The tropical Atlantic SST reached a historical high in 2010, and cooled by 0.33°C from 2010 to 2011 (section 3b). This continued a downward trend in North Atlantic SST since 2006.

After six years of data, a clear seasonal signal is beginning to emerge with a low Meridional Overturning Circulation (MOC) in April and a high MOC in October. The seasonal cycle of the MOC appears to be largely attributed to seasonal vari-

ability in the interior rather than Ekman or Florida current fluctuations. This is being shown as likely due to seasonal upwelling through a direct wind-driven response off Africa (section 3h).

Results for 2010 show the equatorial Pacific (14°N–14°S) was the major source for atmospheric carbon dioxide, emitting about 0.48 Pg C yr^{-1}, and the temperate oceans between 14° and 50° in both hemispheres are the major sink zones, with an uptake flux of 0.70 Pg C yr^{-1} for the northern and 1.05 Pg C yr^{-1} for the southern zone. Both CO_2 effluxes for the El Niño and La Niña periods in the eastern equatorial Pacific are higher than the 29-year mean fluxes. The highest CO_2 effluxes over the past 29 years are due to intensified upwelling of deep water rich in CO_2 caused by an increase of wind speed for 2010.

Details on changes in the patterns of variability from 2010 to 2011 are presented in this chapter. Some sections in this chapter describe the state of the oceans during 2011 whereas others describe 2010 due to lags in availability of quality-controlled data streams. This chapter consists of nine sections describing the ocean climate for 2010 and 2011: (b) Sea surface temperatures, (c) Ocean heat content, (d) Global ocean heat fluxes, (e) Surface salinity, (f) Sub surface salinity, (g) Surface currents, (h) Meridional overturning circulation in the North Atlantic for 2010, (i) Sea level variations, and (j) the global ocean carbon cycle, which is subdivided into sections on air-sea carbon (results mostly for 2010), subsurface carbon inventory (results for 2010), a new section on ocean acidification, and global ocean phytoplankton. Sidebar 3.1 highlights the NASA Aquarius satellite launched June 2011 to study the links between ocean circulation and the global water cycle.

b. Sea surface temperatures—Y. Xue, Z. Hu, A. Kumar, V. Banzon, T. M. Smith, and N. A. Rayner

Sea surface temperatures (SST) play a key role in regulating climate and its variability by modulating air-sea fluxes. In particular, slow variations in SST such as those associated with El Niño-Southern Oscillation (ENSO), the Atlantic multidecadal oscillation (AMO), the Pacific decadal oscillation (PDO), the Indian Ocean dipole (IOD), and the Atlantic Niño, are a source of potential predictability for climate fluctuations on timescales of a season and longer (Deser et al. 2010). A summary of global SST variations in 2011 is provided, with emphasis on the recent evolutions of ENSO, PDO, and IOD, and the 2011 SST is put in the context of the historical record since 1950. To quantify uncertainties in SST variations, three SST products are analyzed: (1) the Optimal Interpolation SST version 2 (OISST; Reynolds et al. 2002), (2) the Extended Reconstructed SST version 3b (ERSST; Smith et al. 2008), and (3) the Met Office Hadley Centre's sea ice and SST dataset (HadISST; Rayner et al. 2003). The weekly OISST is a satellite-based analysis that uses in situ data for bias adjustments of the Advanced Very High Resolution Radiometer (AVHRR) data, which has been available since November 1981. The ERSST and HadISST analyses are historical analyses beginning in the 19th century, and both analyses use statistics developed over the more recent period to extend the SST analysis back in time when in situ observations were sparse. The ERSST includes in situ data only, while the HadISST includes both in situ measurements and AVHRR retrievals from 1982 onwards. Thus, all three SST products represent a "bulk" SST at the depth of the ship and buoy instruments, which can range from less than a meter to several meters from the surface. In this section, SST variations are quantified as SST anomalies (SSTAs) defined as departures from the 1981–2010 climatology (http://www.cpc.ncep.noaa.gov/products/people/yxue/sstclim).

The yearly mean SSTA in 2011 was characterized by below-normal SST in the central and eastern tropical Pacific (Fig. 3.1a), reflecting the La Niña conditions in early 2011 and then again in fall/winter 2011 (see section 4b for detailed descriptions of the La Niña

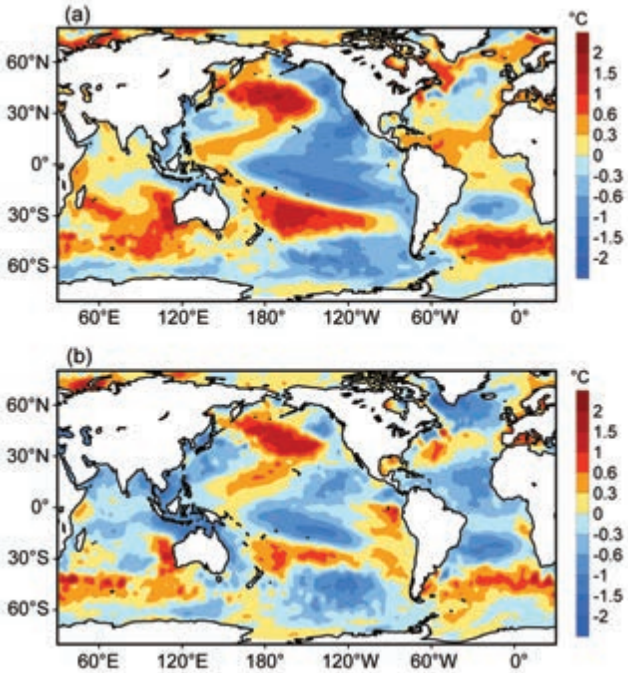

Fig. 3.1. (a) Yearly mean OISST anomaly (°C, relative to 1981–2010 base period) in 2011, (b) 2011 minus 2010 OISST anomaly.

conditions in 2011). The negative SSTAs in the tropical Pacific extended into the subtropics in both hemispheres and along the west coast of North America, and were surrounded by a horseshoe-like pattern of positive SSTAs in the far western tropical Pacific and the central North and South Pacific. The SSTA pattern in the Pacific Ocean resembled the negative phase of the Pacific decacal oscillation (PDO) pattern of Power et al. (1999), while the SSTA in the North Pacific resembled the negative phase of the PDO pattern of Mantua et al. (1997). Negative SSTA was present in the northwest subtropical Pacific and near the Maritime Continent. Outside of the Pacific Ocean, positive SSTA occurred in the western and southern Indian Ocean while alternating positive and negative SSTA prevailed in the North Atlantic.

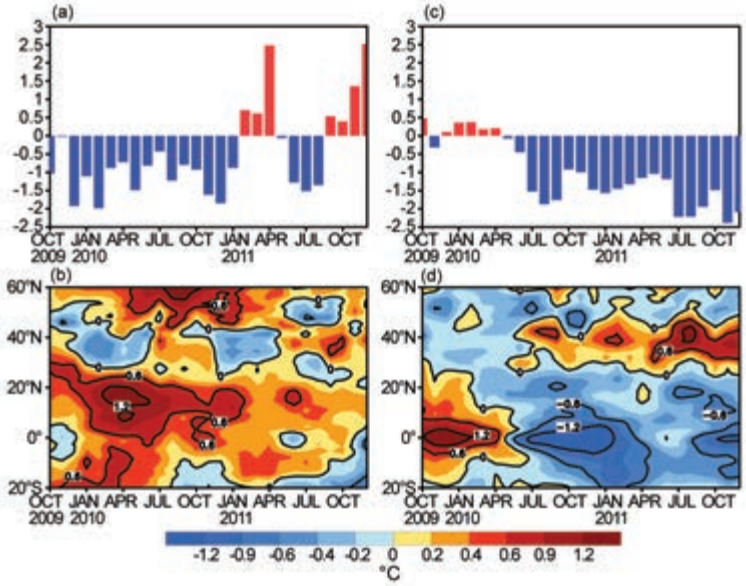

Fig. 3.2. (a) Monthly standardized NAO index from http://www.cpc.ncep.noaa.gov. (b) Time–latitude section of SSTA averaged between 80°W and 10°W. (c) Monthly standardized PDO index. (d) Time–latitude section of SSTA averaged between 160°E and 90°W. SSTA is relative to 1981–2010 base period (°C).

The 2011 minus 2010 SSTA differences show that relative to the previous year, SST cooled substantially across the tropical oceans and warmed in midlatitude oceans (Fig. 3.1b). The cooling in the tropical Pacific was related to the contrast between La Niña conditions in 2011 and a combination of El Niño followed by La Niña conditions in 2010. The warming in the central North Pacific was associated with strengthening of the negative PDO in the second half of 2011 (see Fig. 3.2c). The cooling near the Kuroshio Extension and in the Indo-Pacific region and the tropical Atlantic was likely associated with the remote influences of the 2009/10 El Niño and the 2010/11 La Niña, and will be discussed in detail later in this section. The substantial cooling in the subpolar North Atlantic was probably associated with the evolution of North Atlantic Oscillation (NAO).

The temporal evolution of normalized seasonal mean SSTA in 2011 is shown in Fig. 3.3. The winter 2010/11 (December–February) SSTA was less than -1.5 standard deviation (hereafter referred to as STD) in the central tropical Pacific, indicating a moderate-strength La Niña (Fig. 3.3a). The La Niña conditions weakened during March–May 2011 (Fig. 3.3b) and SSTA returned to near-normal conditions by June–August 2011 (Fig. 3.3c). However, the decline of La Niña did not continue, and a second La Niña (SSTA is < -0.5 STD) reemerged during September–November 2011 (Fig. 3.3d).

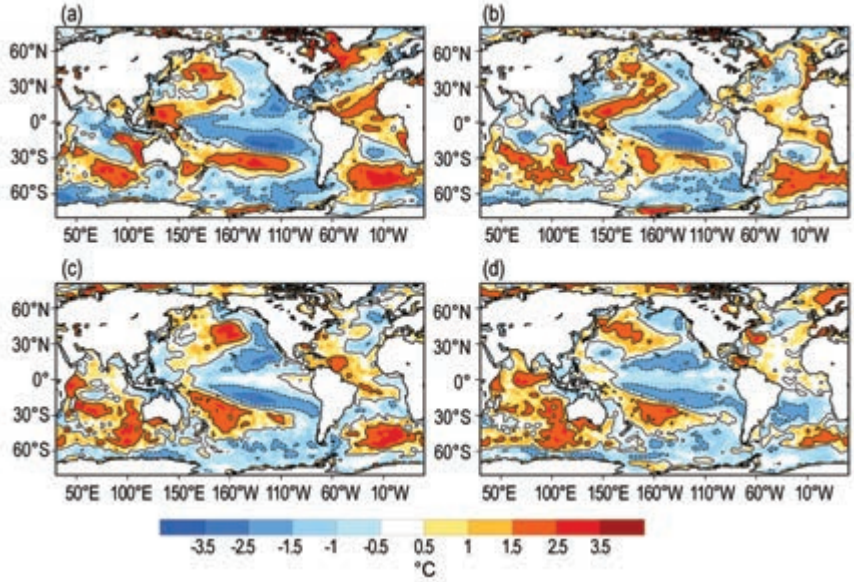

Fig. 3.3. Seasonal mean SSTAs (°C, relative to 1981–2010 base period) for (a) Dec 2010–Feb 2011, (b) Mar–May 2011, (c) Jun–Aug 2011, and (d) Sep–Nov 2011.

Following the peak phase of the La Niña conditions in spring 2011, negative SSTA (< -1.5 STD) emerged in the northwest subtropical Pacific and near the Maritime Continent and the positive SSTA in the tropical North Atlantic weakened substantially (from +1.5 STD to +0.5 STD; Fig. 3.3b). The cooling in the Indo-Pacific region and the tropical Atlantic in spring 2011 may be associated with the remote influences of La Niña. The tropical Indian Ocean and tropical Atlantic are usually cooled after the peak phase of La Niña and warmed after the peak phase of El Niño with a 3–6 month lag (Enfield and Mayer 1997; Klein et al. 1999; Hu et al. 2011). By summer 2011, positive SSTA larger than +1.5 STD emerged in the far western tropical Indian Ocean (Fig. 3.3c). In fall 2011, positive SSTA expanded to the whole tropical Indian Ocean except the area south of Java where negative SSTA persisted in summer and fall. The east-west SSTA gradient resembled the positive phase of the IOD pattern (Saji et al. 1999).

The evolution of SSTAs across the tropical oceans is further analyzed using the time-longitude plot of SSTA averaged in 20°S–20°N from October 2009 to December 2011 (Fig. 3.4). In early 2010, the SST was more than 0.6°C above normal in the eastern tropical Pacific, the western tropical Indian Ocean, and the tropical Atlantic related to the influences of the 2009/10 El Niño. The SST in the tropical North Atlantic actually reached a historical high in April 2010, and this warming has been attributed to the combined effects of the remote influences of the 2009/10 El Niño, persistent negative NAO, and long-term trend (Hu et al. 2011). The yearly mean SSTA in the tropical Indian Ocean also reached a historical high in 2010 (see Fig. 3.5b), probably also due to the combined influences of El Niño and long-term trend.

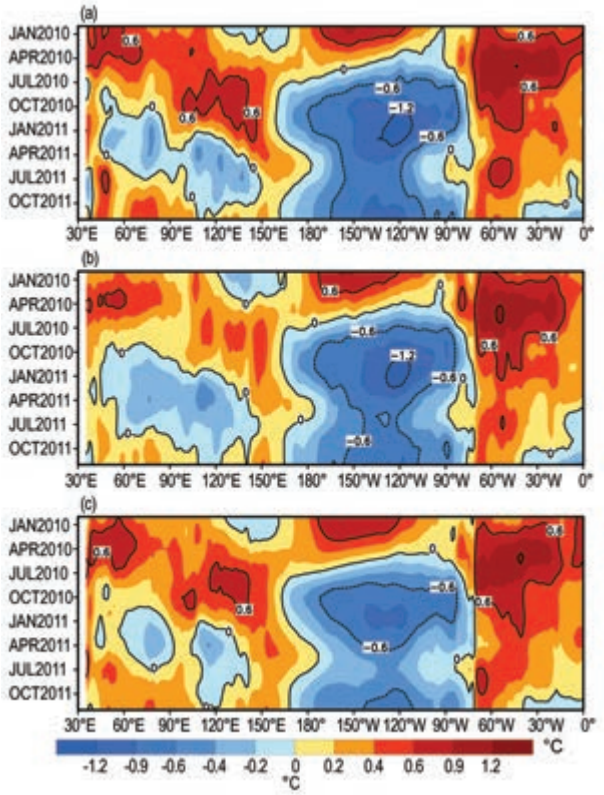

Fig. 3.4. Time–longitude section of SSTA (°C, relative to 1981–2010 base period) averaged between 20°S and 20°N from Oct 2009 to Dec 2011 for the datasets (a) OISST, (b) HadISST, and (c) ERSST.

In the tropical Pacific, there was a fast transition from El Niño to La Niña during spring 2010. At about the same time, SST near the Maritime Continent warmed up and the western Indian Ocean cooled down. This was probably related to the return of the La Niña conditions in the tropical Pacific. The SST near the Maritime Continent was more than 0.6°C above normal according to OISST and ERSST but was 0.3°C above normal based on HadISST. The offset between OISST and HadISST is consistent with what was found in 2010 (Xue et al. 2011, figure 3.5), which might be related to differences in satellite bias correction in the two SST products. It is also noted that the peak value of the negative SSTA in the eastern tropical Pacific was about -1.2°C in OISST and HadISST while it was only -0.9°C in ERSST. Based on a simple comparison of the Niño 3.4 SST, the average SSTA in 5°S–5°N, 170°W–120°W, over the period 1982–2011, ERSST generally underestimates the amplitude of strong SST anomalies associated with ENSO, probably due to the lack of satellite observations and the procedure used for SST reconstruction.

In early 2011 when the 2010/11 La Niña reached its peak phase, negative SSTA emerged in the tropical Indian Ocean. There was an eastward propagation of negative SSTA to the Maritime Continent (Fig. 3.3b). During summer 2011, positive SSTA emerged in the far western tropical Indian Ocean and expanded to the central tropical Indian Ocean in fall 2011. The east-west gradient of SSTA led to establishment of positive IOD conditions in July–October 2011 (see CPC's Monthly Ocean Briefing at http://www.cpc.ncep.noaa.gov/products/GODAS). On the other hand, the tropical North Atlantic SST cooled down substantially in spring 2011 under the remote influences of La Niña conditions, but remained about 0.6°C above normal during the North Atlantic hurricane season that favoreds above-normal hurricane activities.

A tripole SSTA in the North Atlantic, characterized by positive SSTA in the subtropics and high

latitudes and negative SSTA in midlatitudes, persisted from spring 2010 to the winter 2010/11 (Figs. 3.2b, 3.3a). Xue et al. (2011) pointed out that the long persistence of the tripole SSTA was largely forced by persistent negative NAO, which often warms the SST in the subtropics and high latitudes, and cools the SST in midlatitudes by modifying evaporative heat loss from the ocean (Deser and Blackmon 1993). When NAO switched to positive in early spring 2011 (Fig. 3.2a), the tripole SSTA weakened substantially (Fig. 3.3b). In the remaining months of 2011, NAO fluctuated between positive and negative phases and did not provide consistent forcing to the ocean.

The connection between the two-year La Niña cycle and the persistent negative PDO is explored further. The PDO index is calculated as the standardized time series of the projection onto the first empirical orthogonal function (EOF) of monthly ERSST in the North Pacific north of 20°N in the period 1900–93, following the approach of Mantua et al. (1997) in which the global mean SSTA in each month was first removed before the calculation. Zonal average SSTA between 160°E–90°W was used to highlight the evolution of SSTA associated with the PDO. Figure 3.2d shows that positive SSTA emerged in the central North Pacific around June 2010, coincident with the onset of negative phase of the PDO (Figs. 3.2c,d). This also corresponded well with the onset of La Niña around June 2010 in the tropical Pacific. The negative PDO intensified to -1.5 during summer 2010 when the mixed layer depth was the shallowest in the central North Pacific. The PDO weakened slightly and remained at about -1 from October 2010 to June 2011, and then suddenly intensified to be less than -2 in July–August 2011. The strengthening of negative PDO was about one month earlier than the strengthening of negative SSTA in the tropical Pacific in August 2011. It appears that the development of negative PDO around June 2010 and strengthening of negative PDO in July 2011 may not be directly forced by La Niña, although the persistence of negative PDO was probably related to forcings from La Niña. A future study is needed to understand the connections between La Niña and negative PDO.

The historical perspective of the yearly mean SSTA in 2011 is shown in Fig. 3.5 as a basin average

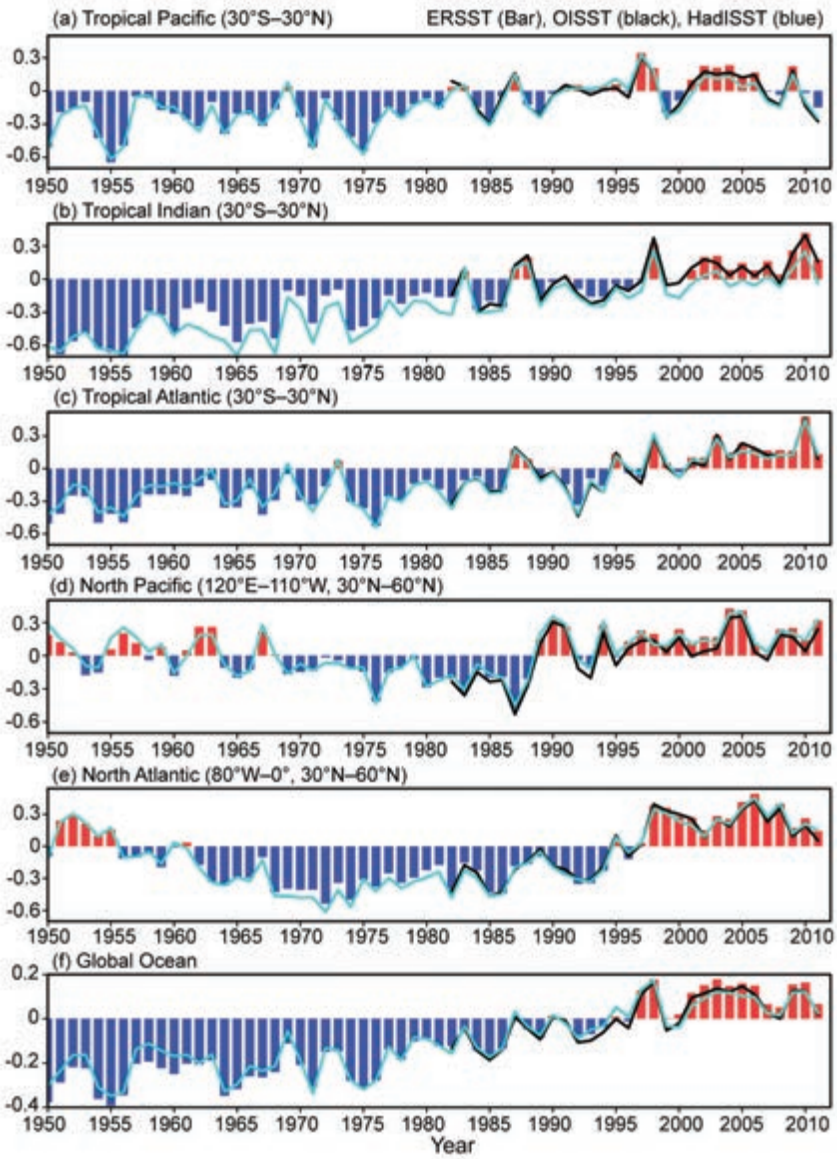

Fig. 3.5. Yearly mean SSTA (°C, relative to 1981–2010 base period) from ERSST (bar) and HadISST (blue line) for 1950–2011 (bar) and OISST for 1982–2011 (black line) averaged over the (a) tropical Pacific, (b) tropical Indian Ocean, (c) tropical Atlantic, (d) North Pacific, (e) North Atlantic, and (f) global ocean.

for the (a) tropical Pacific, (b) tropical Indian Ocean, (c) tropical Atlantic, (d) North Pacific, (e) North Atlantic, and (f) global ocean. The SSTA time series of OISST are largely consistent with those of ERSST in the common period 1982–2011. However, ERSST is generally warmer than OISST, and the difference can reach 0.1°C in some cases. HadISST also agrees well with OISST and ERSST, except it is generally cooler in the tropical Indian Ocean and the differences can reach 0.2°C.

The mean SSTA in the global ocean has a dominant warming trend over which are superimposed interannual variations largely associated with El Niño and La Niña events (Fig. 3.5f). For example, the peaks and valleys in the global ocean SSTA often correspond with those in the tropical Pacific SSTA (Fig. 3.5a). However, the correspondence was not good in 2010, during which the tropical Pacific SST was weakly below normal while the global ocean SST was close to the historical high, which can be attributed to the historical high value in the tropical Indian and tropical Atlantic Ocean. From 2010 to 2011, under the influence of the two-year La Niña cycle, the tropical Pacific SSTA cooled by about 0.14°C (Fig. 3.5a) and became the second coolest year since 1982 ranked using OISST. At the same time, the global ocean SSTA cooled by about 0.1°C (Fig. 3.5f) and became the 12th highest year since 1982.

The tropical Indian Ocean SSTA was dominated by an upward trend with an increase of 0.9°C over the period 1950–2010 when the historical high value was reached (Fig. 3.5b). The interannual variations in the tropical Indian Ocean SSTA corresponded well with those in the tropical Pacific SSTA due to the remote influences of ENSO. From 2010 to 2011, the tropical Indian Ocean SSTA decreased by 0.24°C. In the tropical Atlantic, SSTA increased by 0.33°C from 2009 to 2010 when the historical high value was reached (Fig. 3.5c). From 2010 to 2011, the tropical Atlantic Ocean SSTA decreased by 0.4°C and the cooling tendency was the strongest since 1982. The North Pacific SSTA trended downward from 1950 to 1987, and then rebounded from -0.5°C in 1987 to 0.31°C in 1990, and has been persistently positive since then (Fig. 3.5d). The North Atlantic SSTA trended downward from 1951 to early 1970s, and then trended upward and reached a historical high in 2006. It has been decreasing since 2006 (Fig. 3.5e).

In summary, the 2011 SSTA was characterized by reemergence of the second La Niña in August 2011, strengthening of negative PDO in the second half of 2011, development of positive Indian Ocean dipole in fall 2011, and positive SSTA in tropical North Atlantic. The 2011 minus 2010 SSTA differences show that SST cooled down substantially cross the tropical oceans but warmed up in midlatitudes.

c. *Ocean heat content*—G. C. Johnson, J. M. Lyman, J. K. Willis, S. Levitus, T. Boyer, J. Antonov, and S. A. Good

Storage and transport of heat in the ocean are central to aspects of climate such as El Niño (Zebiak 1989), the North Atlantic Oscillation (Curry and McCartney 2001), hurricanes (Mainelli et al. 2008), sea-level rise (Johnson and Wijffels 2011), the global energy budget (Church et al. 2011), and constraining global warming scenarios (Knutti and Tomassini 2008).

First, an estimate of upper (0 m – 700 m) ocean heat content anomaly (OHCA) for the period 1 January–31 December 2011 (Fig. 3.6a) is discussed, computed from a combination of in situ ocean temperature data (World Ocean Database 2009 – Johnson et al. 2009; and Argo – Roemmich et al.

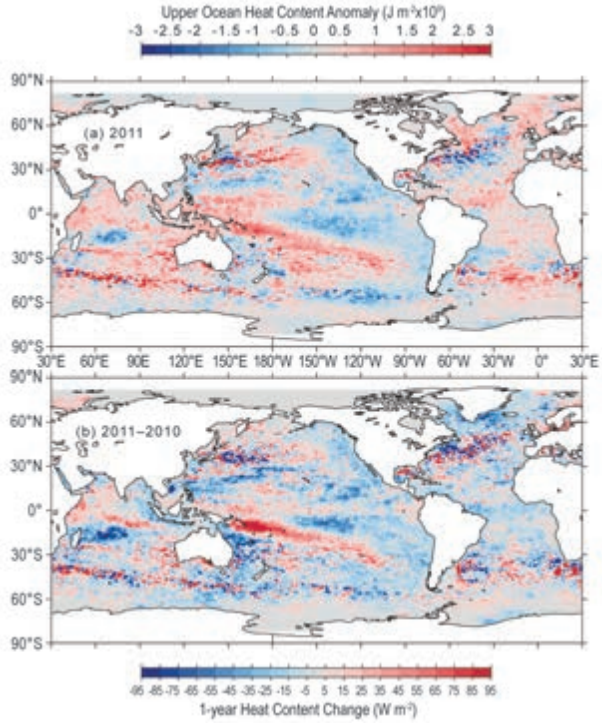

Fig. 3.6. (a) Combined satellite altimeter and in situ ocean temperature data estimate of upper (0 m – 700 m) ocean heat content anomaly OHCA (10^9 J m^{-2}) for 2011 analyzed following Willis et al. (2004), but relative to a 1993–2011 base period. (b) The difference of 2011 and 2010 combined estimates of OHCA expressed as a local surface heat flux equivalent (W m^{-2}). For panel comparisons, note that 95 W m^{-2} applied over one year results in a 3 × 10^9 J m^{-2} change of OHCA.

2009) and satellite altimetry data following Willis et al. (2004), but displayed relative to a 1993–2011 baseline, hereafter the combined estimate. Changes in the combined estimate between 2011 and 2010 (Fig. 3.6b), as well as a map of the linear trend of the combined estimate from 1993 to 2011 and its statistical significance (see Fig. 3.7), are then described. Three different time series of global integrals of in situ only estimates of upper OHCA are presented (see Fig. 3.8). Since OHCA changes are related to depth-integrated ocean temperature changes, increases in OHCA are sometimes referred to below as warming and OHCA decreases as cooling.

In recent years, many of the globally distributed in situ subsurface ocean temperature data are from Argo. Annual estimates of expendable-bathythermograph (XBT) fall rate corrections have been applied for deep and shallow probe data using table 2 of Wijffels et al. (2008), but with no XBT data used after 2005. Details of fields analyzed here may change after more Argo real-time data are subject to delayed-mode scientific quality control, as more data are reported, and as XBT corrections improve.

The combined estimate of OHCA in 2011 (Fig. 3.6a) shows eddy and meander variability down to the 100-km mapping scales, as does, to a greater extent, the difference of the 2011 and 2010 combined estimates (Fig. 3.6b). Strong small-scale spatial variability in OHCA fields is associated with the western boundary currents in every gyre, as well as the Antarctic Circumpolar Current (Fig. 3.6b). The difference in the combined estimates between 2011 and 2010 (Fig. 3.6b) illustrates the large year-to-year variability in regional OHCA, with changes reaching or exceeding the equivalent of a 95 W m^{-2} magnitude surface flux applied over one year (~3 x 10^9 J m^{-2}). For comparison, the global average of incident solar radiation on Earth is ~340 W m^{-2}. Ocean advection likely plays a dominant role in many of these changes.

Local sea level anomalies are the result of OHCA and salinity variability throughout the water column, even to the bottom (e.g., Purkey and Johnson 2010), as well as mass signals (Llovel et al. 2009). Despite this, there are many large-scale visual similarities between the combined estimate of upper OHCA (Fig. 3.6a) and sea level (see Fig. 3.26a) fields in 2011. This similarity reflects both the large contribution of upper OHCA variations to sea-level variations and the influence of the altimeter data in the combined estimate.

Large-scale patterns are evident in the combined estimate of OHCA for 2011 (Fig. 3.6a) and its difference from 2010 (Fig. 3.6b). The pattern of annual mean OHCA (Fig.3.6a) on the equator in the Pacific mostly reflects La Niña conditions, with anomalously low values around the equator in the east and anomalously high values in the west. This pattern is to be expected, since the La Niña that began in early 2010 persisted into 2011 (section 3b).

In 2011, the North Pacific shows an OHCA dipole in the midlatitudes west of 160°E (Fig. 3.6a), perhaps associated with a Kuroshio Extension position southward of the long-term mean. The pattern of anomalous warmth in the central Pacific and cold in the subpolar, eastern subtropical, and eastern tropical Pacific is typical of the negative phase of the Pacific decadal oscillation (PDO; Mantua et al. 1997) and La Niña. The band of high OHCA in the South Pacific that extends from the Solomon Islands in the west to about 40°S west of Chile (Fig. 3.6a) has been present at various latitudes since 2006 (see previous *State of the Climate* reports). This year, it migrated several degrees south of its 2010 position, as seen in the north-south dipole in year-to-year OHCA (Fig. 3.6b), and is associated with anomalous zonal currents in 2011, as well as the change since 2010 (see Fig. 3.17). Wind stress curl changes between 2010 and 2011 (see Fig. 3.10b) are well correlated with this shifting band, as are positive salinity anomalies both surface (see Fig. 3.12) and subsurface (see Fig. 3.14).

Except for a cold anomaly patch centered around 15°S, 75°E, in 2011 the Indian Ocean was mostly higher in OHCA than the base period (Fig. 3.6a). This cold anomaly is associated with a positive anomaly in sea surface salinity (see Fig. 3.12).

In the subpolar North Atlantic, the Labrador Sea remained high in OHCA in 2011 (Fig. 3.6a), although it cooled quite a bit since 2010 (Fig. 3.6b). This ocean cooling is consonant with an increasing NAO index since the very low values in the winter of 2009/10. The continued high OHCA values in the eastern subpolar North Atlantic (Fig. 3.6a) suggest that subtropical influences are strong there (e.g., Johnson and Gruber, 2007), consistent with anomalously salty surface conditions in that region in 2010 (see Fig. 3.12). In 2011, a band of low OHCA was still present in the region of the Gulf Stream Extension (Fig. 3.6a), as it was in 2010. This band is consistent with a southward shift of that current (see Fig. 3.17), expected given the low NAO index in the winter of 2009/10 (e.g., Taylor and Stephens 1998). While the tropical Atlantic mostly cooled from 2010 to 2011 (Fig. 3.6b) it remained warmer than the 1993–2011 average (Fig. 3.6a).

A few distinct (Fig. 3.7a) and statistically significant (Fig. 3.7b) regional patterns stand out in the

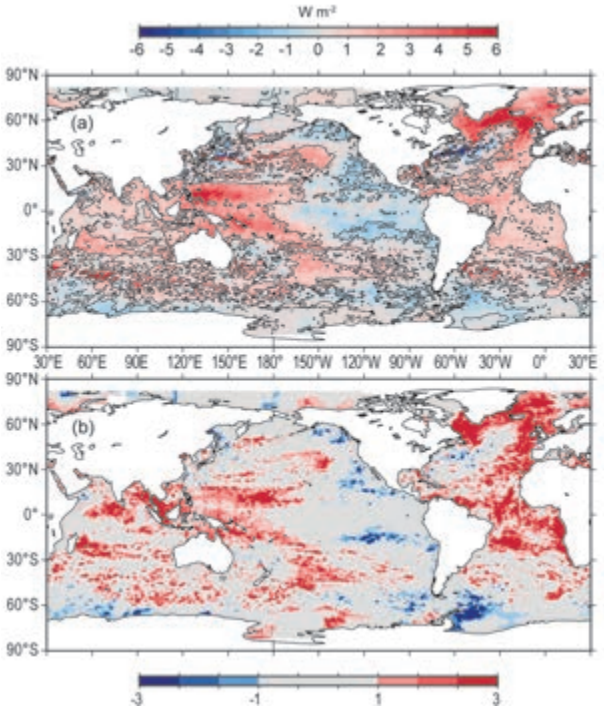

Fig. 3.7. (a) Linear trend from 1993 to 2011 of the combined satellite altimeter and in situ ocean temperature data estimate of upper (0 m–700 m) OHCA (W m^{-2}) analyzed following Willis et al. (2004). Areas with statistically significant trends are outlined in black. (b) Signed ratio of the linear trend to its 95% uncertainty estimate, with increasing color intensity showing regions with increasingly statistically significant trends.

1993–2011 OHCA local linear trends. In the Indian Ocean, the warming trend was widespread and statistically significant in many locations.

In the Atlantic Ocean, the Labrador, Irminger, and Greenland-Iceland-Norwegian Seas have all trended warmer over 1993–2011 (Fig. 3.7a), reflecting a robust regional warming trend over the interval despite the cooling from 2010 to 2011 (Fig. 3.6b). These changes may be owing to an overall decrease in the NAO index from 1993 to 2011. Eastern portions of the Atlantic also trended warmer across both hemispheres. Areas with warming trends in the Atlantic are widespread, including highly statistically significant trends in eastern portions of both hemispheres. Cooling trends are limited in the Atlantic to the Gulf Stream Extension, probably related to a southward shift in that current, also expected with an overall declining NAO index.

Statistically significant (Fig. 3.7b) 1993–2011 regional trends in the Pacific Ocean (Fig. 3.7a) include warming in the western tropical Pacific and extratropical cooling in the east, consistent (via the geostrophic relation) with general strengthening of the interior subtropical-tropical circulation attributed to trade wind intensification (Merrifield and Maltrud 2011). The statistically significant warming in the central North Pacific and cooling south of Alaska and off the west coast of North America are also consistent with an overall downward trend in the PDO index from 1993 to 2011. There is a similar-looking trend pattern in the South Pacific.

The overall 1993–2010 trends in Southern Ocean OHCA were towards warming, consistent with previous analyses (e.g., Böning et al. 2008), but with some local cooling trends on both sides of the Antarctic Peninsula and near Antarctica in the Indian Ocean (Fig. 3.7a).

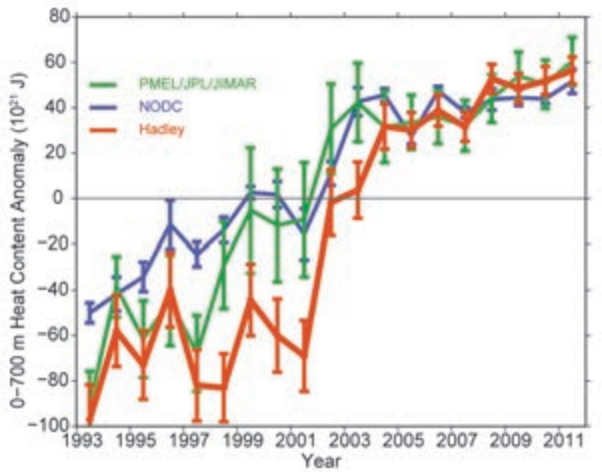

Fig. 3.8. Time series of annual average global integrals of in situ estimates of upper (0 m–700 m) OHCA (10^{21} J, or ZJ) for 1993–2011 with standard errors of the mean. The NODC estimate (http://www.nodc.noaa.gov/OC5/indprod.html) follows Levitus et al. (2009). Uncertainties are estimated solely from the variance of quarterly estimates of OHCA. The PMEL/JPL/JIMAR estimate is a weighted integral (Lyman and Johnson 2008) using Argo and WOD 2009 (Johnson et al. 2009) data with the Wijffels et al. (2008) Table 2 XBT bias adjustments applied and no XBT data after 2005. Uncertainty estimate methodology follows Lyman et al. (2010). The Hadley estimate applies XBT bias adjustments from Table 1 of Wijffels et al. (2008) to the EN3 dataset (Ingleby and Huddleston 2007; http://www.metoffice.gov.uk/hadobs) and is computed from estimates of monthly OHCA following Palmer et al. (2007). Uncertainty estimate methodology follows Palmer and Brohan (2011) but adds uncertainty in the XBT bias correction. For comparison, all estimates have been individually offset (vertically on the plot), first to their individual 2004–11 means (the best sampled time period), and then to their collective 1993–2011 mean (the record length).

Three different upper ocean estimates (0 m – 700 m) of globally-integrated in situ OHCA (Fig. 3.8) reveal a large increase in global integrals of that quantity since 1993. While levels appear to be increasing more slowly since around 2003 or 2004 than over the previous decade, the sum of the mass and thermal expansion components of the global sea level budget agree with observed sea-level rise rates since at least 2005 (see Fig. 3.28). The highest values for each global OHCA estimate are for 2011, although uncertainties only permit statistically significant trends to be estimated over about ten years or longer (Lyman 2011). Interannual details of the time series differ for a variety of reasons, including differences in climatology, treatment of the seasonal cycle, mapping methods, instrument bias corrections, quality control, and other factors (Lyman et al. 2010). Some of these factors are not taken into account in some of the displayed uncertainties, so while the error bars shown do not always overlap among the three estimates, they are not necessarily statistically different from each other. However, all three curves agree on a significant warming of the upper ocean since 1993, accounting for a large portion of the global energy imbalance over this time period (Church et al. 2011).

d. Global ocean heat fluxes—L. Yu, P. W. Stackhouse Jr., and R. A. Weller

The net heat flux (Qnet) at the ocean surface is the sum of the four air-sea heat transfer processes: shortwave radiation (SW), longwave radiation (LW), latent heat (LH), and sensible heat (SH) fluxes. Solar radiation is the ultimate heat source for the Earth. About 47% of the total solar radiation reaching the Earth is absorbed by the surface ocean and land (Trenberth et al. 2009). Of the energy absorbed by the ocean, some is radiated back to the atmosphere by LW, some is transformed into SH and LH and released to the atmosphere through conduction and evaporation, and the remaining energy is either transported by currents or stored and sequestered in the ocean. Knowing how these heat exchange processes balance at the ocean surface and how much the net residual heat flux has changed are fundamental to the understanding of the role of the ocean in mitigating radiative perturbations and modulating the global climate.

Daily estimates of LH and SH on 1° grids over the global oceans are routinely produced by the Objectively Analyzed air-sea Fluxes (OAFlux) project (http://oaflux.whoi.edu) at the Woods Hole Oceanographic Institution (Yu and Weller 2007). The computation of the OAFlux products uses the state-of-the-art bulk flux algorithm version 3.0 developed from the Coupled Ocean-Atmosphere Response Experiment (COARE; Fairall et al. 2003), with the surface meteorological variables determined from an optimal blending of satellite retrievals of surface wind and temperatures and surface meteorology from reanalysis/forecast models. The accuracy of the OAFlux LH and SH estimates was evaluated using 120-plus buoys available over the global oceans (Yu et al. 2008). The averaged root-mean-square (rms) differences between OAFlux and buoy over the buoy locations are 9.6 W m^{-2} (8%) for LH and 2.6 W m^{-2} (15%) for SH. The OAFlux project also develops global daily vector wind analysis from synergizing passive radiometer wind speed retrievals and radar scatterometer vector wind retrievals (Yu and Jin 2012, manuscript submitted to *J. Geophys. Res.*). The wind analysis for the post-QuikSCAT (after November 2009) period uses satellite measurements from the Special Sensor Microwave Imager/Sounder (SSMIS), the Advanced Scatterometer (ASCAT) aboard the EUMETSAT METOP satellite, and the WindSat (a passive polarimetric microwave sensor) aboard the Department of Defense Coriolis satellite.

Global daily surface SW and LW flux products on 1° grids are now delivered in near real-time (within one week) by the CERES (Clouds and Earth's Radiant Energy Systems) Fast Longwave And SHortwave Radiative Fluxes (FLASHFlux) project (http://flashflux.larc.nasa.gov) at the NASA Langley Research Center (Stackhouse et al. 2006). This output data product is made possible by processing Terra and Aqua observations from CERES and cloud property retrievals from the Moderate-resolution Imaging Spectroradiometer (MODIS) using simplified calibration assumptions with fast radiation algorithms (Kratz et al. 2010). Evaluation of the FLASHFlux surface radiation with ground measurements from the Surface Radiation Budget Network (SURFRAD) stations shows an rms error of 29.3 W m^{-2} (15.7%) for downward SW and 18.6 W m^{-2} (6.0%) for downward LW.

The annual mean Qnet in 2011 produced by combining FLASHFlux and OAFlux datasets is displayed in Fig. 3.9 (next page). An area-weighted spatial mean of 25 W m^{-2} was removed to adjust global mean balance. The regions of net heat gain (positive Qnet) and net heat loss (negative Qnet) are in broad agreement with the climatological mean pattern (Josey et al. 1999). The tropical oceans receive an excess of heat energy owing to the high rate of insolation throughout the year, and the strongest heating (> 140 W m^{-2}) is located on the equator in the eastern Pacific. The

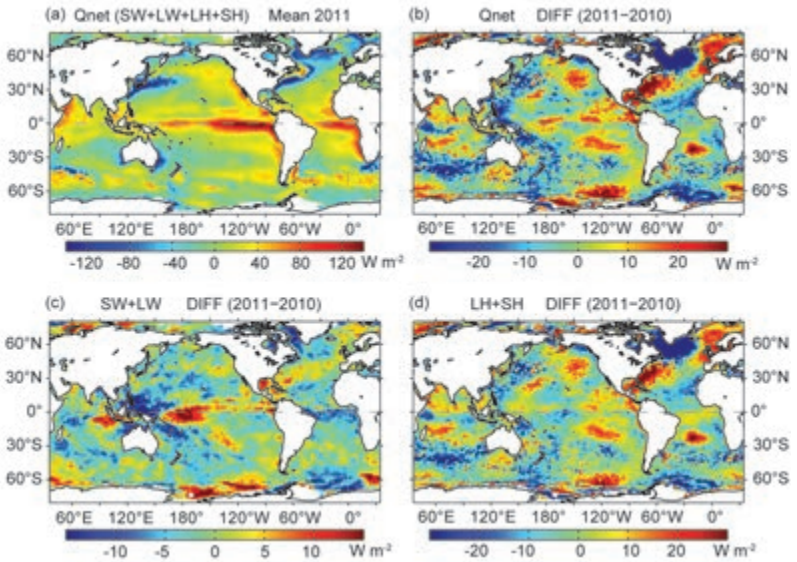

Fig. 3.9. (a) Annual mean net heat flux (W m^{-2}) into the ocean (Qnet) in 2011. Positive (negative) values denote ocean heat gain (loss). (b) Annual mean difference in Qnet between 2011 and 2010. The 2011 minus 2010 mean difference in surface radiation (SW+LW) and turbulent heat fluxes (LH+SH) are shown in (c) and (d), respectively. In (b)–(d), positive (negative) values denote where the ocean gained more (lost less) heat in 2011 compared to 2010.

subtropics and high latitudes experience net heat loss to the atmosphere, with the maximum heat loss (< -140 W m^{-2}) occurring over the western boundary currents (WBCs) in the northern midlatitudes. The primary mechanism of the large net heat loss in the vicinity of the WBCs is latent and sensible heat fluxes in the fall and winter seasons, during which the cold and dry air masses advected from the lands by strong westerly winds induce sharp air-sea temperature and humidity contrasts, intensifying latent and sensible heat release to the atmosphere.

The 2011 minus 2010 difference plot of Qnet (Fig. 3.9b) shows organized large-scale changes in net heat flux into the global oceans. One marked change was observed in the North Atlantic, characterized by a tripole structure with an area of significant negative anomalies (more ocean heat loss) in the Labrador and Irminger Seas between 45°N and 65°N, a band of positive anomalies (more ocean heat gain) in the midlatitudes centered over the Gulf Stream pathway and stretching northeastward to the Norwegian Sea, and a band of negative anomalies (more ocean heat loss) in the subtropics between the equator and 30°N. The tripole pattern reflected the atmospheric conditions of a generally more positive NAO phase in 2011 compared to the persistently negative phase in 2010 (see Fig. 3.2). The anomaly pattern of surface net radiation SW+LW (Fig. 3.9c) was very similar to that of LH+SH (Fig. 3.9d), but LH+SH accounts more for the magnitude of Qnet anomalies. This is in good agreement with the study of Cayan (1992) that, in the extratropical oceans, the variance in SW and LW is small and Qnet is dominated by the variance of LH and SH.

The North Atlantic tripole pattern is also seen in the 2011 minus 2010 wind speed difference field (Fig. 3.10a), but with opposite signs. The 2011 mean wind vectors is superimposed to help characterize the change in prevailing winds. Compared to 2010, there was a strengthening of westerlies across the midlatitudes on a more northerly track and a strengthening of trade winds in the tropical Atlantic. The pattern is consistent with past positive NAO phase (Hurrell 1995; Visbeck et al. 2001). It can be observed that enhanced LH+SH (negative anomalies in Fig. 3.9d) occurred in regions of strengthened wind speeds (positive anomalies). Similarly, the regions of weakened LH+SH (positive anomalies) coincided with the regions of weakened wind speeds (negative anomalies). Wind direction

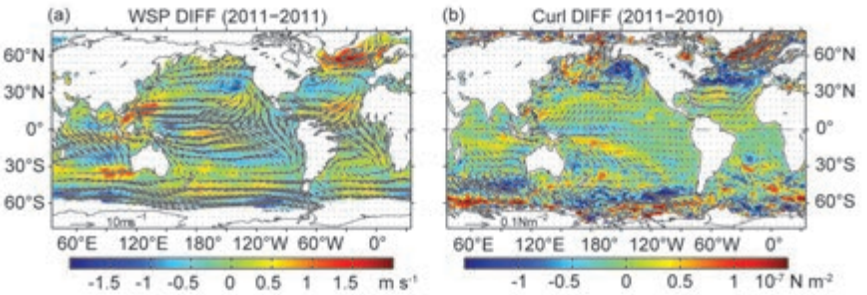

Fig. 3.10. (a) Differences between the 2011 and 2010 wind speed at 10-m height (colored background), with the 2011 mean wind vector superimposed (black arrows). Positive (negative) values denote a strengthening (weakening) of prevailing winds compared to 2010. (b) Differences between the 2011 and 2010 wind stress curl (colored background), with the wind stress vector differences between 2011 and 2010 superimposed (black arrows). Positive (negative) values denote anticyclonic (cyclonic) curl anomalies.

is also important. For instance, the excessive turbulent heat loss in the Labrador and Irminger Seas resulted from both the intensified subpolar cyclonic wind circulation and the cold and dry air advected to the region by the westerlies. It is known that the basin-scale NAO SST variability is driven primarily by the atmospheric forcing via the effects of LH+SH, mixing, and the wind-driven Ekman currents (Cayan 1992; Deser and Blackmon 1993). The 2011 surface warming tendency of the North Atlantic Ocean from 2010 corresponded well with positive (more ocean heat gain) Qnet anomaly and concurring negative (weakened) wind anomaly. Meanwhile, the regional surface cooling tendency also correlated well with negative (more ocean heat loss) Qnet anomaly and positive (strengthened) wind anomaly. The North Atlantic is clearly an example that surface net heat flux is a forcing for SST anomalies.

Surface heat flux plays a dual role in dynamics of large-scale SST anomalies. While it contributes to the generation of SST anomalies in the North Atlantic, surface heat flux also responds to the SST anomalies that have been generated from other processes and can act to oppose those anomalies. The latter role of Qnet is displayed in the Pacific and Indian Oceans. The sea surface in the eastern part of the Pacific in 2011 was dictated by a developing La Niña in the tropics and negative PDO phase in the North Pacific. Compared to 2010, colder SST anomalies appeared over the central tropical Pacific between 160°E and 120°W with a center on the equator near the date line (see Fig. 3.1). In general, the upper OHCA year-to-year tendency also appears to be damped by year-to-year changes in Qnet. Unlike the North Atlantic where negative SST anomalies were well correlated with negative Qnet anomalies, the negative SST anomalies here were associated with positive Qnet anomalies that can be attributed primarily to the LH+SH component. In the tropics, ENSO SSTs are governed by ocean dynamics through wind-driven upwelling of cold water from the thermocline (Wyrtki 1981). The cooler ocean surface led to a weaker evaporative heat loss, which together with enhanced downward radiation, resulted in more downward Qnet. In the tropical Indian Ocean, SST anomalies follow the ENSO index. As the regional sea surface cooled from 2010 to 2011, an increase in Qnet, owing to reduced evaporative heat loss and enhanced radiation, was also observed. These positive Qnet anomalies acted as a damping to the existing negative SST anomalies, suppressing the growth of ENSO-induced SSTs.

Consistent with past La Niña events (Ropelewski and Halpert 1989), the western Pacific warm pool and deep tropical convection in 2011 were retracted to the far west of the date line. As a result, the convection across the Maritime Continent was enhanced. The increased cloudiness led to a reduction of downward SW+LW by more than 10 W m^{-2} and dominated the change of Qnet in the region. Away from the convergence center in both zonal directions, convection was suppressed in both directions, resulting in large increase in SW+LW (> 15 W m^{-2}) across the central equatorial Pacific and eastern Indian Oceans. Corresponding change in wind was evident, with weaker wind speed in the center of convergence and enhanced equatorial westerlies in the Indian Ocean and enhanced easterlies near the date line. The change in wind speed governed the change in LH+SH in the warm pool (Zhang and McPhaden 1995). It can be seen that the tropical western Pacific and eastern Indian Oceans were regions where the SW+LW anomalies compensated the LH+SH anomalies in producing the Qnet anomalies. In other regions such as the eastern Pacific and North Atlantic, the SW+LW anomalies worked in concert with the LH+SH anomalies to increase the Qnet anomalies.

In the North Pacific, Qnet served primarily as a forcing for the PDO SSTs, and the anomalies of the two variables have the similar sign. In the southern oceans between 30°S and 50°S, the Qnet anomalies were overwhelmingly negative due to the increased heat loss by LH+SH in response to positive SST anomalies. The changing relationships between Qnet and SST with the ocean basins demonstrate that the global climate system is ruled by intricate feedbacks between the ocean and the atmosphere.

Overall, yearly variability of Qnet over the global oceans is attributable more to variability of LH+SH.

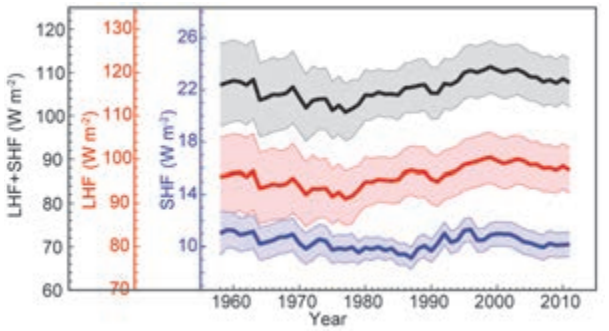

Fig. 3.11. Year-to-year variations of global averaged annual mean latent flux plus sensible heat flux (LHF+SHF; black curve), LHF (red curve), and SHF (blue curve). The shaded areas indicate the error bars of the flux estimates at the 95% confidence level.

The long-term perspective of the change in 2011 LH+SH is shown in the annual mean time series averaged over the global oceans from 1958 to 2011 (Fig. 3.11). The 2011 LH+SH was slightly down from the 2010 mean, continuing the downward trend that started around 2000. A tendency toward reversing the upward trend that characterized the decades of 1980s and 1990s is thus indicated. The 54-year time series displays decadal oscillations dominated by LH, with a low at 99 W m^{-2} in 1977 and a high at 109 W m^{-2} in 1999. It is worth noting that LH is not only an important component in the global heat and energy balance but also a key component of the freshwater flux over the oceans that contributes to the change of ocean surface salinity (see Fig. 3.13).

e. *Sea surface salinity*—G. C. Johnson and J. M. Lyman

Ocean storage and transport of freshwater are intrinsic to aspects of global climate, including the water cycle (e.g., Schanze et al. 2010), El Niño (e.g., Maes et al. 2006), and anthropogenic climate change (e.g., Held and Soden 2006). Only since 2004 has the advent of Argo (an array of profiling floats that measures temperature and salinity year-round in the upper 2 km of the ice-free global ocean, nominally at 10 day intervals and 3°× 3° spacing; Roemmich et al. 2009) allowed an annual assessment of global upper ocean salinity and its complement, freshwater.

The near-global Argo data are used to determine near-global annual average bulk (viz. near-surface, as opposed to skin) sea surface salinity (SSS) anomalies for 2011 relative to a long-term climatology, describe how annual SSS anomalies have changed in 2011 relative to 2010, and assess 2004–11 SSS trends and their statistical significance. The data, downloaded from an Argo global data assembly center in January 2012, are a mix of real time (preliminary) and delayed mode (scientific quality-controlled). The estimates presented here could change after all the data have been subjected to careful scientific quality control, and as other data sources (e.g., Aquarius satellite, Sidebar 3.1) are integrated into the estimates.

The shallowest salinity value flagged as good from each Argo profile is used in this analysis, generally at 9-m depth, with some as shallow as 4 m, and those with depth > 25 m are excluded. These data are subjected to a statistical check to discard extreme outliers, defined as points within a 3°-radius of a grid point with temperature or salinity values three times the interquartile range above the third or below the first quartiles. After this check, the remaining data are cast as differences from climatological monthly mean surface salinity fields from the World Ocean Atlas 2009 (WOA 2009; Antonov et al. 2010). The resulting anomalies are objectively mapped (Bretherton et al. 1976) for each year using a covariance function combining a 6° (latitude and longitude) length-scale Gaussian with a 9° length-scale exponential and a noise-to-signal variance ratio of 2.2.

Climatological SSS patterns are correlated with surface freshwater flux [the sum of evaporation, precipitation, and river runoff (e.g., Beránger et al. 1999)] but horizontal and vertical advection and mixing are also important in many locations, at least on seasonal time scales (Yu 2011). In each ocean basin, subtropical salinity maxima centered between roughly 20° and 25° in latitude (Fig. 3.12, grey contours) are signatures of the predominance of evaporation over precipitation. Conversely, in most regions where climatological surface salinities are relatively fresh, such as the

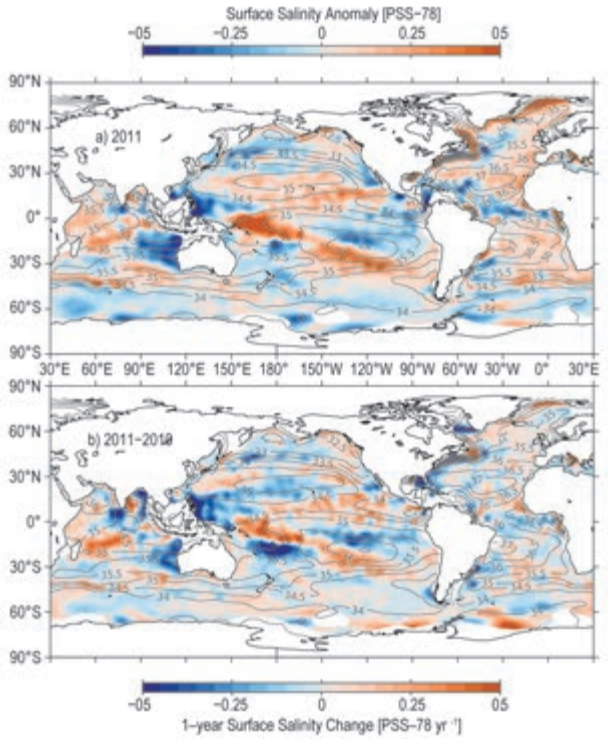

Fig. 3.12. (a) Map of the 2011 annual surface salinity anomaly estimated from Argo data [colors in 1978 Practical Salinity Scale (PSS-78)] with respect to monthly climatological salinity fields from WOA 2009 (yearly average, gray contours at 0.5 PSS-78 intervals). (b) The difference of 2011 and 2010 surface salinity maps estimated from Argo data [colors in PSS-78 yr^{-1} to allow direct comparison with (a)]. White ocean areas are too data-poor to map. While salinity is often reported in practical salinity units, or PSU, it is actually a dimensionless quantity reported on the PSS-78.

high latitudes and the intertropical convergence zones (ITCZs), precipitation generally dominates over evaporation.

The 2011 SSS anomalies (Fig. 3.12a, colors) reveal some large-scale patterns that also hold in 2004 through 2011. The regions around the subtropical salinity maxima are on balance salty with respect to WOA 2009. Most of the high-latitude climatologically fresh regions appear fresher than WOA 2009, including in the vicinity of the Antarctic Circumpolar Current near 50°S and in the western subpolar gyre of the North Pacific. These patterns are consistent with an intensified hydrological cycle (that is, more evaporation in drier locations, and more precipitation in rainy areas), as seen in simulations of global warming. These simulations suggest this signal might be discernible over the last two decades of the 20th century (Held and Soden 2006), consistent with the multiyear nature of these anomalies. While anomalous ocean advection could influence the SSS pattern over decadal time scales, changes observed at the local extrema are presumably relatively insensitive to such effects because horizontal gradients there are minimal. This SSS anomaly pattern and its interpretation are consistent with other analyses (Hosoda et al. 2009; Durack and Wijffels 2010). Changes in ocean interior salinity values also appear consistent with an increase in the hydrological cycle (Helm et al. 2010; section 3f).

In contrast to some other high-latitude areas, the subpolar North Atlantic and Nordic Seas in 2011 were mostly anomalously salty with respect to the historical WOA 2009 climatology (Fig. 3.12a, colors), as they have been since at least 2004 (see previous *State of the Climate* reports). The salty anomaly in this region is consistent with a stronger influence of subtropical gyre waters in the northeastern North Atlantic in recent years coupled with a reduced extent of the subpolar gyre (Häkkinen et al. 2011). On the basin scale, the North Atlantic loses freshwater to the atmosphere whereas the North Pacific gains it (Schanze et al. 2010), so the changes here may again be consistent with an increased hydrological cycle (Durack and Wijffels 2010).

Sea surface salinity changes from 2010 to 2011 (Fig. 3.12b, colors) strongly reflect 2011 anomalies in precipitation (see Fig. 2.21 and Plate 2.1i), and to a lesser extent year-to-year changes in evaporation, with the latter being closely related to latent plus sensible heat flux changes (see Fig. 3.9d). Advection by anomalous ocean currents (see Fig. 3.17) also plays a role in sea surface salinity changes. For instance, prolonged La Niña conditions over the last few years, associated with an anomalously strong Indonesian Throughflow (England and Huang 2005), may be partly responsible for the freshening observed northwest of Australia, as the throughflow does bring relatively fresh water into the Indian Ocean. Precipitation anomalies in this region, while consistent with freshening, are not large (see Fig. 2.21 and Plate 2.1i). The South Pacific convergence zone also appears to have shifted south from 2010 to 2011, consistent with the dipole in salinity changes centered around 10°S in the southwest tropical Pacific. Farther to the southeast, the apparent southward shift in the subtropical surface salinity maximum is associated with year-to-year changes in the ocean heat content (see Fig. 3.6b), so the salty shift is associated with a warm shift.

There are also correspondences between the surface salinity changes from 2010 to 2011 and subsurface changes over the same period (see Figs. 3.14, 3.15, 3.16). Some of the surface changes are confined mostly to the upper one or two hundred meters, including many of those in the tropics. However, others apparently extend deep into the water column, suggesting influences of shifting ocean currents and fronts. Deeper-penetrating changes are found in the high southern latitudes, near the Antarctic Circumpolar Current, and in the North Atlantic, near the Gulf Stream Extension and the North Atlantic Current.

Trends from 2004 through 2011 are estimated by local linear fits to annual average SSS maps (Fig. 3.13a), as are the ratio of these trends to their 95% significance (Fig. 3.13b). The starting year is 2004, when Argo coverage became near-global. The most striking trend patterns are in the Pacific and Indian Oceans. Saltier surface values in the western and central tropical Pacific extend into the eastern Pacific subtropics in both hemispheres. Some freshening also occurs in the western subtropics of each hemisphere in the Pacific and around the Philippine Sea, extending into the Indian Ocean northwest of Australia (the latter again perhaps owing to the La Niña of the past few years). Large-scale freshening is also evident in the eastern tropical South Pacific. These recent trends differ from the previously reported 50-year trends discussed above. The differences are not surprising given the very different time periods over which the trends are computed.

SIDEBAR 3.1: AQUARIUS SATELLITE MISSION PROVIDES NEW, DETAILED VIEW OF SEA SURFACE SALINITY—G. LAGERLOEF, F. WENTZ, S. YUEH, H.-Y. KAO, G. C. JOHNSON, AND J. M. LYMAN

The Aquarius satellite mission (http://aquarius.nasa.gov), launched on 10 June 2011, has been measuring sea surface salinity (SSS) from space since 25 August 2011. Aquarius's primary scientific goal is to study links among the ocean circulation, the global water cycle, and climate by measuring ocean surface salinity (Lagerloef et al. 2008). Recent multidecadal SSS trends provide a strong indication of changes in the global water cycle, with wetter areas gaining in rainfall and low rainfall regions becoming more arid (see section 3e; also Gordon and Giulivi 2008). Aquarius data will allow analyses of these changes at higher spatial and temporal resolution than presently possible with the in situ SSS observing system (Figs. SB3.1-3). Aquarius will complete a year of measurements in autumn 2012, allowing the start of detailed exploration of the annual coupling of SSS, rainfall, surface currents, and sinks such as subduction and vertical mixing. Aquarius data in subsequent years will improve annual cycle statistics, yield new information on ENSO and other interannual climate variations, and advance our understanding of the marine freshwater budget (Lagerloef et al. 2010).

Sea surface salinity data from Aquarius and the previously launched European Soil Moisture Ocean Salinity (SMOS) mission (http://www.esa.int/smos; Font et al. 2004; Lagerloef and Font 2010) provide a fundamentally new ocean remote sensing capability. The Aquarius microwave sensor, built by NASA, is the prime instrument on the joint United States and Argentina Aquarius/SAC-D observatory. The Argentine Comisión Nacional de Actividades Espaciales (CONAE) developed the Satélite de Aplicaciones Científicas (SAC-D) spacecraft, which carries Aquarius and other scientific sensors.

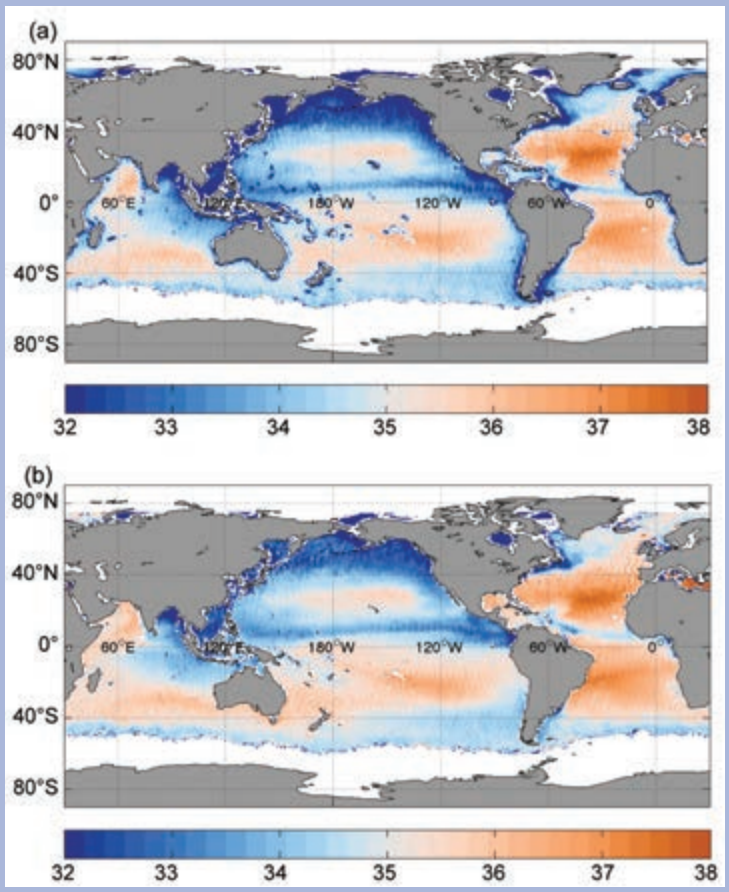

Fig. SB3.1. (a) Mean global map of the first four months (Sep–Dec 2011) of Aquarius satellite sea surface salinity (PSS-78) measurements omitting a land correction (see text) near coastlines and using an optimized combined active-passive algorithm of Yueh and Chaubell (2012). (b) Same as (a) but with the land correction applied, and using the present roughness correction that combines NCEP operational analysis winds and Aquarius scatterometer data. Data are interpolated to 0.5° grid resolution, and Aquarius data have a 150-km smoothing scale applied.

Salinity remote sensing involves measuring the ocean's surface microwave emission at 1.413 GHz (in the L-band portion of the spectrum protected for radio astronomy). This emission is modulated by the electrical conductivity of seawater, hence salinity, of the top few cm. Aquarius also measures radar backscatter at 1.26 GHz, to mitigate the emission variations due to surface roughness (Yueh et al. 2010; Le Vine et al. 2007), the largest error source in the salinity retrieval. Aquarius provides seven-day global coverage and is designed to achieve a monthly average global root-mean-square (rms) measurement error less than 0.2 (PSS-78) at 150-km resolution (Lagerloef et al. 2008).

Aquarius composite four-month mean (September–December 2011) global SSS maps, using two experimental processing algorithms (Figs. S3.1a.b), differ mainly in the inclusion of the land correction and also in their methods of surface roughness correction. The size of the Aquarius footprint limits the accuracy for measurements close to coastal boundaries where the land emission adds a negative bias for which a land correction has been developed. The data without the correction (Fig. SB3.2a) exhibit a spurious low-salinity shadow along

the continental boundaries that is absent in the image with the correction applied (Fig. SB3.2b). This land correction appears to be effective and will continue to be studied and improved. Both the land and roughness corrections in Fig. SB3.2b are part of the present baseline data processing. Subtle differences between these images in the ocean interior, far from the coast, are associated with a slight difference in roughness correction. Data where wind speed is greater than 15 m s^{-1} and SST is less than 5°C have been ignored in these figures because the SSS retrievals are not yet reliable under those conditions.

An SSS map derived from Argo data for the same four-month period (Fig. SB3.2a), objectively analyzed as described in section 3e shows the same predominant large-scale and well-known climatological ocean salinity features that can be seen in both Aquarius maps. These features include higher salinity in the subtropics versus lower salinity in high-precipitation belts near the equator and at high latitudes, an Atlantic Ocean that is generally saltier than the Pacific, as well as the striking salty-fresh contrast between the Arabian Sea and the Bay of Bengal.

Differences between the Aquarius and Argo maps (Fig. SB3.2b) highlight some important features. The Aquarius Southern Ocean SSS values are biased high relative to the Argo fields. This bias is actively under study, and is partly associated with high winds and low surface temperatures that complicate the retrieval processing. In the tropics, however, the Aquarius data reveal important details at spatial and temporal scales that Argo does not resolve, such as prominent low-salinity water associated with outflow from the Amazon and Orinoco Rivers, and the sharper and better-defined SSS gradients around the intertropical convergence zones (ITCZ) of both the Atlantic and Pacific. In addition, the shallowest salinity measurements for most Argo floats, often between 4 m and 10 m, may miss surface-intensified, highly-stratified fresh pools from precipitation and river outflows found in low wind conditions. The two data sources are highly complementary, with Argo data vital for analyzing and correcting biases in Aquarius SSS data and Aquarius data resolving temporal and spatial SSS variability missed by Argo.

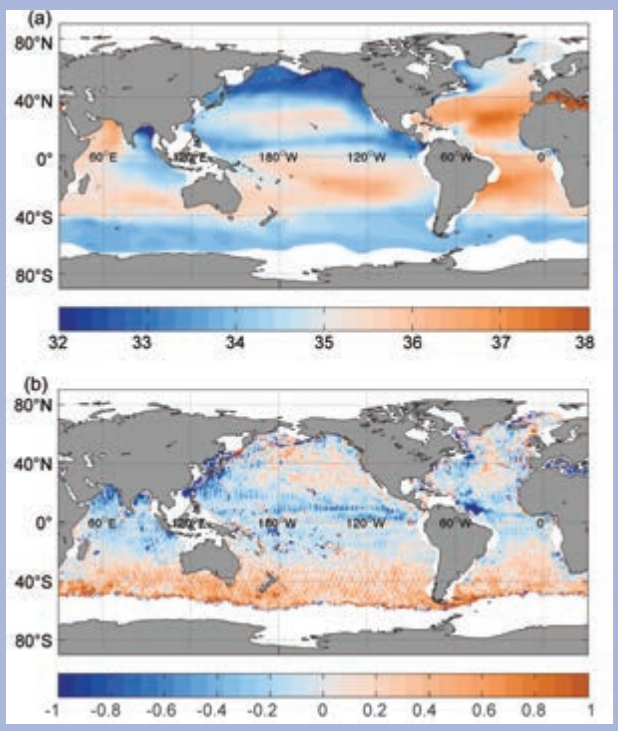

Fig. SB3.2. (a) Objectively analyzed Argo SSS for the same four-month period as Fig. SB3.1. (b) The difference between the Aquarius data in Fig. SB3.1b minus the Argo map in (a). Crosshatch patterns are parallel to the orbit path and are attributed to small residual calibration differences that are currently under investigation.

A seven-day composite of Aquarius SSS with current vectors overlaid across most of the North Pacific ITCZ (Fig. SB3.3) illustrates the close relation between surface currents (Dohan and Maximenko 2010) and SSS patterns associated with the narrow, meandering, eastward-flowing North Equatorial Counter Current (NECC). Such newly resolved detail of SSS, not as evident from spatially smoother SSS maps constructed from in situ data alone, will allow new insights about the interactions among net air-sea freshwater flux, ocean currents, and SSS. Unvalidated Aquarius data are presently available for evaluation, and the first validated data will be released in December 2012.

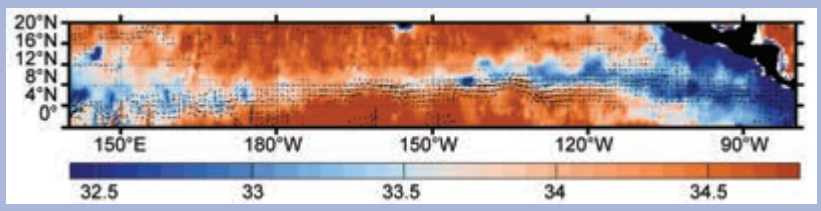

Fig. SB3.3. A 7-day (29 Aug–04 Sep) snapshot of a portion of the Pacific low salinity region within the ITCZ showing small-scale salinity structure related to surface current meanders and eddies. Aquarius data are interpolated to 0.33°-grid resolution, surface currents are 1° resolution.

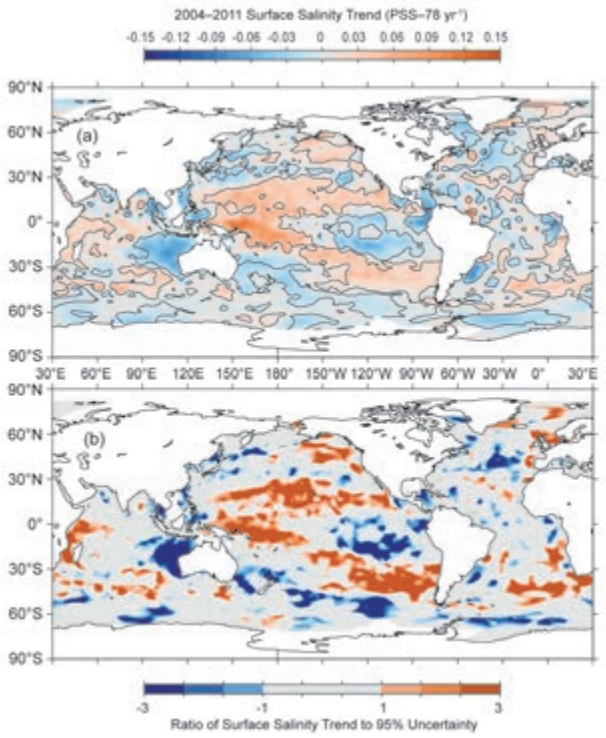

Fig. 3.13. (a) Map of local linear trends estimated from annual surface salinity anomalies for 2004–11 from Argo data (colors in PSS-78 yr^{-1}). (b) Signed ratio of the linear trend to its 95% uncertainty estimate, with increasing color intensity showing regions with increasingly statistically significant trends. White ocean areas are too data-poor to map.

f. Subsurface salinity—T. Boyer, S. Levitus, J. Antonov, J. Reagan, C. Schmid, and R. Locarnini

Mixed layer salinity and evaporation minus precipitation (E–P) are well correlated in many parts of the world's oceans (Yu 2011). Since E–P is difficult to accurately measure over the ocean, it has been proposed that near-surface salinity could be used to constrain E–P estimates, acting as a sort of rain gauge (Schmitt 2008; Yu 2011). Durack and Wijffels (2010) have shown that E–P surface forcing has led to an intensification of the global hydrological cycle over the last 50 years, exemplified by increasing salinity at the sea surface in areas dominated by evaporation and decreasing surface salinity in areas dominated by precipitation. These surface-forced changes extend to subsurface levels. Globally-averaged near-surface waters have increased in salt content in recent times compared to long-term means, while intermediate waters have decreased in salt content (Roemmich and Gilson 2009; Helm et al. 2010). These changes can have major implications for water mass composition and circulation patterns. Investigating interannual and long-term variability of subsurface salinity, in conjunction with sea surface salinity (SSS) and surface fluxes, can improve understanding not only of changes in the ocean, but also changes in the atmosphere affecting the global climate system.

The method used to investigate changes to subsurface salinity was to use all available subsurface ocean salinity profile data for year 2011 and construct 1° gridded fields of salinity anomalies at different depths from these data for comparison with similarly calculated fields from 2010 and the long-term mean salinity field. The majority of data used in this analysis are from the Argo profiling float program (Roemmich et al. 2009). For 2011, 121 414 Argo salinity profiles were recorded, the majority of which extend from the near surface to 2000-m depth. The geographic distribution of these data includes most of the ice-free ocean with bottom depth deeper than 2000 m. Only 14 682 of these profiles have yet undergone rigorous Argo scientific quality control because at least six months of data from the same Argo float subsequent to a profile's date are needed for proper drift analysis. However, more than half of the non-delayed mode (real-time) data were adjusted, if necessary, based on knowledge of the salinity drift for a float that was obtained during the scientific quality control done on earlier float cycles. In addition to the Argo data, 32 662 profiles of daily averaged salinity at different depths down to 750 m from the TAO/TRITON (Pacific), PIRATA (Atlantic), and RAMA (Indian) Equatorial Ocean moored buoy arrays were included. A total of 10 274 real-time ship-based on conductivity temperature depth (CTD) salinity profiles, obtained through the Global Temperature and Salinity Profile Project (GTSPP), were also used in this analysis. Data from a few additional cruises were provided by the International Council for the Exploration of the Seas (ICES), the CLIVAR program, and the New Zealand Ministry of Fisheries. A final contribution to the analysis is 30 825 salinity profiles from gliders, also obtained through GTSPP. These glider data are regional, with many profiles in a limited area over a short time period. However, the geographic regions are diverse: the western North Pacific Ocean, around Australia, the Mediterranean Sea, tropical Atlantic Ocean, Gulf of Mexico, and coastal North Pacific Ocean. Additional scientific quality control was performed on all salinity and salinity anomaly data as per Boyer et al. (2009). Data from 2010 were reanalyzed to account for the increased number of delayed mode Argo data (52 124 of 112 642 profiles) and additional CTD data (4439 profiles). The 2010 fields

did not change significantly with regards to large-scale patterns from the fields used in the 2010 *State of the Climate* analysis (Levitus et al. 2011). All data and quality control flags used in the present analysis are available through the World Ocean Database (Boyer et al. 2009). All calculated fields are available at http://www.nodc.noaa.gov/OC5/3M_HEAT_CONTENT/.

The above described salinity data were analyzed as follows: Individual profiles of observed salinity were interpolated to 26 standard levels from the surface to 2000-m depth. Each standard level value was subtracted from the appropriate World Ocean Atlas (WOA; Antonov et al. 2010) long-term mean monthly salinity value for the 1° geographic grid box in which the salinity profile was taken. This removes the annual salinity cycle, leaving salinity anomaly profiles relative to the long-term mean. Salinity anomalies were bin averaged over the 1° grid boxes for each standard depth. The binned mean salinity anomalies are then objectively analyzed (Antonov et al. 2010) to generate a salinity anomaly value for each 1° ocean grid box at each standard depth from the surface to 2000 m, or the ocean bottom, whichever is encountered first. The 12 analyzed monthly salinity anomaly fields are averaged at each standard depth to produce an annual mean salinity anomaly field on a 1° global field for each depth level. This process is followed for years 2010 and 2011. The gridded 1° mean anomalies were averaged along each 1° latitude belt separately for the Atlantic, Pacific, and Indian Oceans. Zonal mean salinity anomalies for 2011 compared with the long-term mean are shown along with the zonal mean difference between salinity for 2011 and 2010. The latter give an indication of interannual change between the two years, while the former provides the context via a comparison with long-term salinity change patterns. A Student's *t* test was performed on all zonal mean anomalies at each standard depth. The mean anomalies are significant for all values > 0.1 (red and blue shading in Fig. 3.14) at the 99% level. For comparison with SSS and to understand upper ocean salinity in more detail, analyzed salinity anomaly values at each depth level in the upper 100 m for each 1° grid box were averaged using volume weighting to give a mean salinity anomaly for the upper 100 m. This mean salinity anomaly of the upper 100 meters exhibits the same large-scale patterns of positive and negative salinity anomaly as Fig. 3.12a, with reduced amplitude.

The Pacific Ocean zonal mean salinity difference between 2011 and the long-term mean (Fig. 3.14a) reveals long-term freshening of the water column of the southern high latitudes (e.g., Böning et al. 2008) to depths > 1000 m and as far north as 35°S. Meijers et al. (2011) attribute the freshening in this area to southward movement of the Antarctic Circumpolar Current and water mass changes possibly due to increased precipitation and ice melt. There was little change in the salinity anomaly in this region from 2009 to 2010 (Levitus et al. 2011) and an increase in salinity near 60°S from 2010 to 2011 (Fig. 3.14b) illustrates the year-to-year variability about the long-term trend. The increased salinity in the upper 200 m between 40°S and the equator, interrupted by a band of freshening between 20°S and 10°S, evident in the 2011 salinity anomaly compared with the long-term mean was reinforced from 2010 to 2011, with the exception of the near surface (upper 50 m) salinity north of 10°S. Figure 3.12a (in section 3e) shows that the reason for this banding is, generally, salinification in the top 100 m in the western South Pacific and freshening in the eastern South Pacific from 40°S to the equator, with the freshening in the east weaker except in the area 20°S to 10°S. Figure 3.12a also shows very strong salinification under the SPCZ which intensified from 2010 to 2011, with salinification > 0.1 to depths of 400 m. This interannual change effectively counters the pattern of subsurface freshening propagating from the south seen between 2009 and 2010. In both

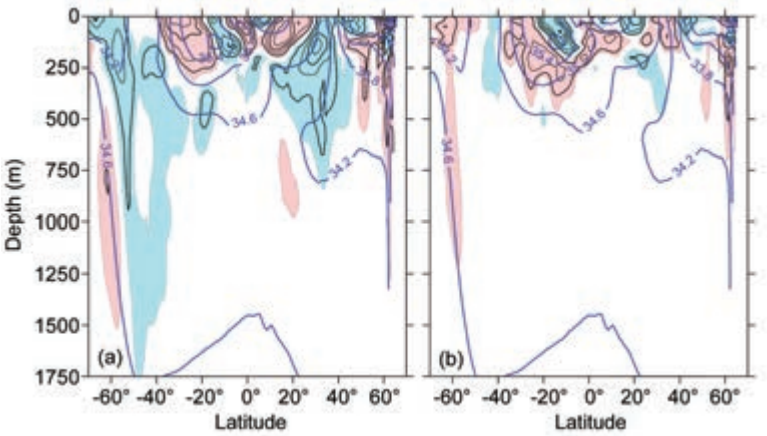

Fig. 3.14. Zonally averaged (a) 2011 salinity anomaly and (b) 2011 minus 2010 salinity field for the Pacific Ocean. Blue shading represents negative (fresh) anomalies < -0.1, red shading represents positive (salty) anomalies > 0.1. The contour interval for the anomalies is 0.2. In the background of each figure (thick blue contours) is the zonally averaged climatological mean salinity (Antonov et al. 2010). Contour intervals for the background are 0.4. All values are on the PSS.

2010 and 2011, the North Pacific was saltier in the upper 200 m than the long-term average between 20°N and 30°N (Fig. 3.14a; Levitus et al. 2011), counter to the trend shown in Boyer et al. (2005) for 1955 to 1998, and it was fresher in the main thermocline for the subtropics down to 600 m. The latter is a continuation of the trend described in Ren and Riser (2010). Except for changes in the high southern latitudes, differences between 2010 and 2011 in the Pacific were > 0.2, mainly in the upper 300 m of the water column. The salinity changes from 2009 to 2010 in the Pacific were also confined to the upper 300 m (Levitus et al. 2011).

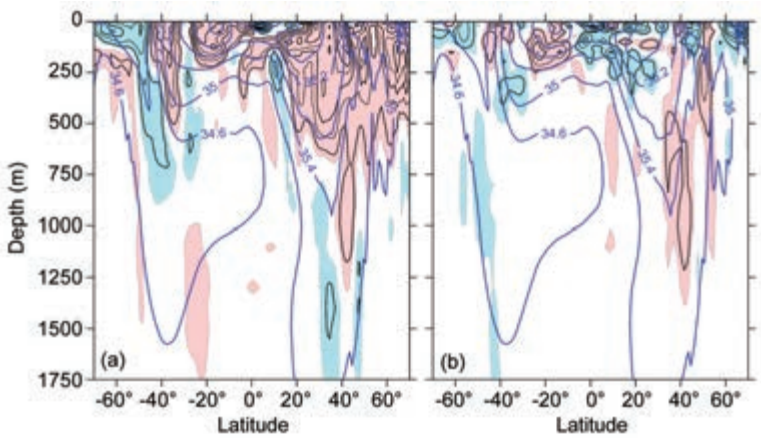

Fig. 3.15. Zonally averaged (a) 2011 salinity anomaly and (b) 2011 minus 2010 salinity field for the Atlantic Ocean. Blue shading represents negative (fresh) anomalies < -0.1, red shading represents positive (salty) anomalies > 0.1. The contour interval for the anomalies is 0.2. In the background of each figure (thick blue contours) is the zonally averaged climatogical mean salinity (Antonov et al. 2010). Contour intervals for the background are 0.4. All values are on the PSS.

An increase of salinity in the subtropical and tropical North Atlantic and a decrease in salinity in the subpolar North Atlantic has been described from the mid-1950s through the mid-1990s (Curry et al. 2003; Boyer et al. 2007; Wang et al. 2010). More recently, both the subpolar North Atlantic and the subtropic North Atlantic have become saltier (Boyer et al. 2007; Wang et al. 2010). The 2011 analysis (Fig. 3.15a) is consistent with these patterns. The 2011 Atlantic zonal mean salinity anomalies exhibit deep (> 500 m) large-scale increases (> 0.2) in salinity over most of the North Atlantic compared with the long-term mean. In the South Atlantic, salinification is confined mainly north of 40°S, deeper than 400 m to 30°S, reaching only to 200 m from that latitude to the equator. Freshening to depths > 500 m is found in the Atlantic, similar to the Pacific, south of 40°S. The near-surface signature of this freshening is stronger in the Atlantic than the Pacific in the high southern latitudes. The zonal mean salinity for 2011 minus 2010 shows a general year-to-year freshening across much of the Atlantic in the upper 100 m (Fig. 3.15b). Figure 3.12, section 3e, reveals a more patchy distribution of small positive and negative anomalies between the two years, with general freshening along the equator and in the western North Atlantic. The freshening along the equator extends to 300 m. Deeper down, the larger freshening that occurred between 2009 and 2010 to 1000 m, 30°N to 40°N (Levitus et al. 2011), reversed in 2010 to 2011, with salinification > 0.2 from 500 m to > 1000 m in this area.

In the Indian Ocean, mean zonal salinity anomalies for 2011 (Fig. 3.16a) for the high southern latitudes (> 45°S) were fresher from the surface to > 1000 m than the long-term mean, except for latitudes farther south of 60°S, which were fresher only in the upper 100 m of the water column, and more saline at deeper levels. This is the same pattern seen in the Pacific

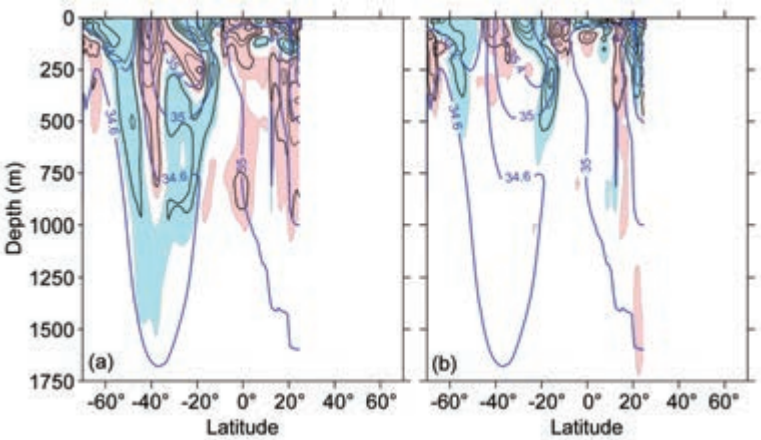

Fig. 3.16. Zonally averaged (a) 2011 salinity anomaly and (b) 2011 minus 2010 salinity field for the Indian Ocean. Blue shading represents negative (fresh) anomalies < -0.1, red shading represents positive (salty) anomalies > 0.1. The contour interval for the anomalies is 0.2. In the background of each figure (thick blue contours) is the zonally averaged climatogical mean salinity (Antonov et al. 2010). Contour intervals for the background are 0.4. All values are on the PSS.

and Atlantic basins as well. The Indian Ocean was also fresher in the upper 200 m from 30°S to 10°S, and from 300 m to 1000 m in roughly the same latitude span. The latitude band from 45°S to 30°S was more saline down to 700 m, with a subsurface extension northward to almost 10°S that reaches as deep as 300 m. North of 10°S, most of the water column is more saline than the long-term mean. Much of the freshening in the Indian Ocean, outside high southern latitudes, is in the eastern Indian extending westward from the west coast of Australia (see Fig. 3.12). Comparing 2011 to 2010 (Fig. 3.16b), the freshening in the band 15°S–35°S was more intense between the two years than between 2009 and 2010 (Levitus et al. 2011), to depths of 500 m. In the western Indian Ocean, there was a large (> 0.2) increase in salinity from 20°S to the equator which is confined to the upper 200 m. In the North Indian Ocean, the eastern Arabian Sea and eastern Bay of Bengal were fresher compared to the year before (Fig. 3.12), with this freshening dominating the zonal mean salinity anomalies down to 400 m.

g. *Surface currents*—R. Lumpkin, G. Goni, and K. Dohan

This section describes ocean surface current changes, transports derived from ocean surface currents, and features such as rings inferred from surface currents. Surface currents are obtained from in situ and satellite (altimetry and wind) observations.

Near-surface currents are measured in situ by drogued satellite-tracked drifting buoys and by current meters on moored buoys (see Appendix 2 for specific dataset information). During 2011, the drifter array ranged in size from a minimum of 352 drogued buoys to a maximum of 576, with a median size of 416 drogued drifters (undrogued drifters continue to measure SST, but are subject to significant wind slippage; Niiler et al. 1987). The moored array included 36 buoys with current meters, all between 16°S and 21°N. These tropical moorings compose the TAO/TRITON (Pacific; 16 buoys with current meters reporting in 2012), PIRATA (Atlantic; 6 buoys) and RAMA (Indian; 14 buoys) arrays.

Global fields of ocean currents are estimated using two methodologies, both using the AVISO Ssalto/Duacs multimission altimeter near-real time gridded product. The first is a synthesis of AVISO with in situ drifter measurements and reanalysis winds (Niiler et al. 2003), which adjusts the altimeter-derived geostrophic velocity anomalies to match the observed in situ eddy kinetic energy. The second is the purely satellite-based OSCAR (Ocean Surface Current Analyses-Real time) product, which uses AVISO altimetry, winds, SST, and the Rio05 mean dynamic topography (Rio and Hernandez 2004) to create 1/3°-resolution surface current maps averaged over the 0 m – 30 m layer of the ocean (Bonjean and Lagerloef 2002). In both cases, anomalies are calculated with respect to the time period 1992–2007. Ocean transports are derived from a combination of sea height anomaly (from altimetry) and climatological hydrography.

Global zonal current anomalies and changes in anomalies from 2010 are shown in Fig. 3.17 and discussed below for individual ocean basins.

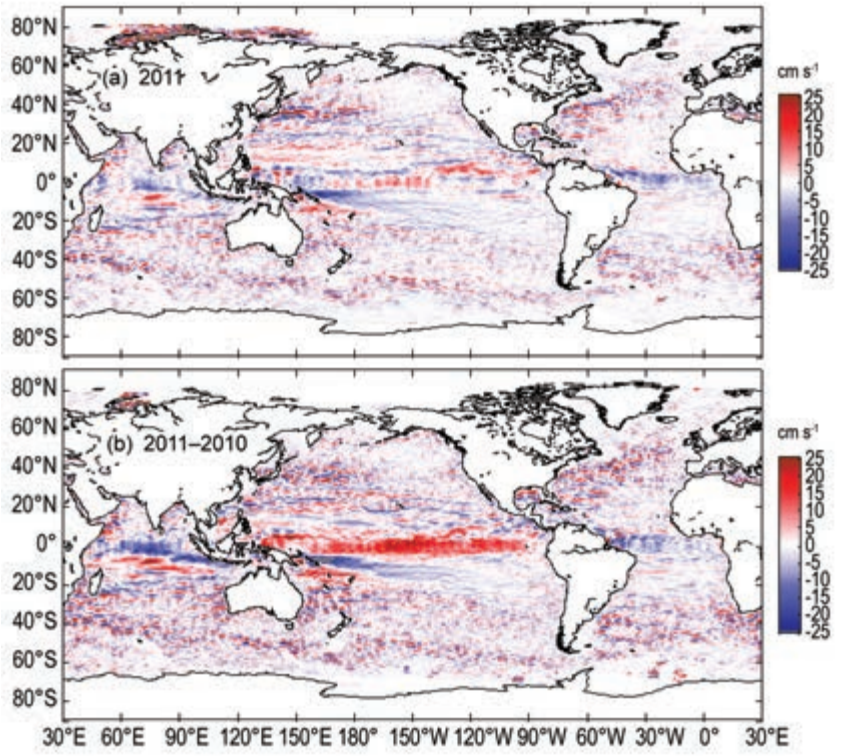

Fig. 3.17. Global zonal geostrophic anomalies (cm s^{-1}) for (a) 2011 and (b) 2011 minus 2010 derived from a synthesis of drifters, altimetry, and winds.

1) Pacific Ocean

In the tropical Pacific, 2011 began with surface currents near their climatological January values. This changed dramatically by February, however, with eastward anomalies developing from the South American coast to ~170°W, with maxima of 30 cm s^{-1} – 40 cm s^{-1} in the band 100°W–150°W. By March, the eastward equatorial anomalies spanned the basin. They persisted in strength in April, and then weakened quickly in May. By June, large-scale surface currents had returned to their climatological values. During the peak of this event in March–April, eastward anomalies peaked at 30 cm s^{-1} – 40 cm s^{-1} at 110°W to 170°E. These surface current anomalies, with their associated advection of warm SST, acted to quickly erase the La Niña (cold) SST anomalies in the eastern tropical Pacific that had persisted since 2010 (Fig. 3.18; see also section 3b), yielding near-neutral values for the Niño 3, 3.4, and 4 indices by midyear.

In July 2011, westward equatorial anomalies of 10 cm s^{-1} – 20 cm s^{-1} began developing at 110°W–160°W. This anomalous pattern expanded westward through August and September, at which point westward anomalies of 15 cm s^{-1} – 20 cm s^{-1} were seen from ~100°W to the western edge of the basin. By October, the pattern began weakening in the band 160°W–170°E, and by November the pattern was much patchier, with westward anomalies dominant only in the band 90°W–160°W. In December, westward anomalies of 15 cm s^{-1} – 25 cm s^{-1} again developed in the western Pacific, in the band 130°W–160°E.

Because of the alternating signs of zonal current anomalies in early vs. late 2011, annual mean zonal anomalies (Fig. 3.17) are not as dramatic as they were in 2010 (a predominantly La Niña year for zonal current anomalies). The 2010 anomalies dominate 2011 minus 2010 (Fig. 3.17b).

Surface current anomalies in the equatorial Pacific typically lead SST anomalies by several months, with a magnitude that scales with the SST anomaly magnitude. Recovery to normal current conditions is also typically seen before SST returns to normal. Thus, current anomalies in this region are a valuable predictor of the evolution of SST anomalies and their related climate impacts. This leading nature can be seen clearly in the first principal empirical orthogonal function (EOF) of surface current (SC) anomaly and separately of SST anomaly in the tropical Pacific basin (Fig. 3.18). In the altimetry time period 1993–2011, the maximum correlation between SC and SST is R=0.68 with SC leading SST by 81.1 days. In 2011, the most dramatic feature of this mode was the extremely rapid change in the SC anomaly from negative values in late 2010 to El Niño-like (positive) values in early 2011. This switch in the sign of the SC anomaly happened as the SST anomaly reached its strongest negative value (Fig. 3.18); for the next few months, while the SC anomaly remained positive, the negative SST anomaly decreased in magnitude. In the latter half of 2011, the SC anomaly returned to neutral-to-La Niña-like (negative) values, leading the return of cold SST anomalies by several months (Fig. 3.18). It is interesting to note that, unlike earlier years, a positive SST anomaly did not follow the positive SC anomaly in early 2011; this is likely due to the extreme magnitude of the 2010 La Niña SST anomaly (the most negative value in this time series) and the relatively brief duration of the positive SC anomaly in 2011.

In the *State of the Climate in 2010*, it was noted that the Kuroshio exhibited a narrower and stronger annual mean signature, and shifted approximately 1° in latitude to the north compared to 2006–09. This pattern continued through 2011, with no large-scale pattern in the 2011 minus 2010 difference (Fig. 3.17b) indicating a shift in

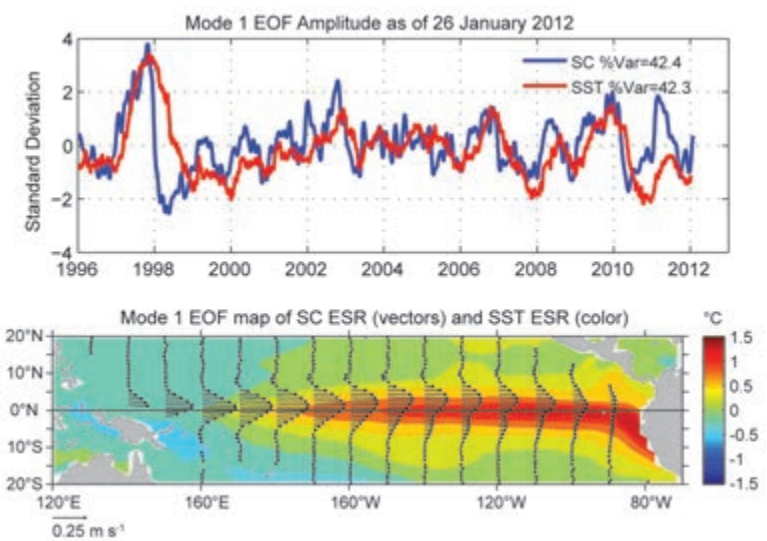

Fig. 3.18. Principal empirical orthogonal functions (EOF) of surface current (SC) and SST anomaly variations in the tropical Pacific from the OSCAR model. (Top) Amplitude time series of the EOFs normalized by their respective standard deviations. (Bottom) Spatial structures of the EOFs.

the Kuroshio Extension latitude with respect to 2010.

2) Indian Ocean

In January 2011, westward equatorial anomalies of ~20 cm s^{-1} were seen in the central Indian Ocean (75 °E–90°E), north of a band of eastward anomalies at 50°E–100°E, 10°S. The westward equatorial anomalies persisted through June, with the pattern shifting westward through this period. In July, eastward equatorial anomalies of 10 cm s^{-1} – 20 cm s^{-1} developed at 60°E–85°E; this pattern weakened and shifted to the west in August, and was extremely weak in September when westward equatorial anomalies again developed in the center of the basin. These anomalies developed in intensity through November, reaching peak values of 30 cm s^{-1} – 40 cm s^{-1} in November at 65°E–75°E. They then rapidly weakened, and December saw a return to near-normal climatological surface current values across the basin at large scales. In the annual mean (Fig. 3.17), westward anomalies dominated the basin in 2011, in contrast to the weak eastward anomalies of 2010.

The shedding of eddies from the Agulhas Current into the Atlantic basin as seen in altimetry remained at its climatological value. The transport of the Agulhas can be estimated by combining sea height anomaly and climatological hydrography; in 2011, the transport of the Agulhas decreased by ~5 Sv (Sverdrup, equal to 10^6 m^3 s^{-1}, a unit commonly used for ocean volume transports) with respect to the 2010 mean, with much weaker values seen for the second half of 2011 (Fig. 3.19). A dramatic, brief maximum of 84 Sv was observed at the beginning of 2011, exceeding all previous maxima observed since 1993.

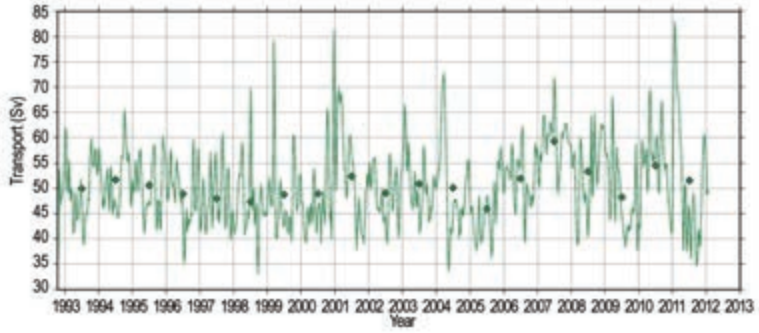

Fig. 3.19. Transport of the Agulhas Current from a combination of sea height anomaly and climatological hydrography (http://www.aoml.noaa.gov/phod/altimetry/cvar/agu/index.php).

3) Atlantic Ocean

In the first few months of 2011, the tropical Atlantic basin did not exhibit any basin-wide zonal surface current anomalies, although westward anomalies tended to dominate near the equatorial band east of ~30°W. Through boreal spring to summer, these relatively weak westward equatorial anomalies expanded across the basin. These anomalies persisted through September and October, and intensified in November to 10 cm s^{-1} – 20 cm s^{-1} at 20°W–30°W. The overall annual mean anomaly (Fig. 3.17) was westward in 2011, similar to the 2010 pattern.

In the Gulf of Mexico, surface current speed anomalies of 30 cm s^{-1} – 35 cm s^{-1} were present along and north of the climatological Loop Current path in 2011. An overall increase in the Loop Current strength is not likely, as the measured transport of the Florida Current between Florida and the Bahamas increased by less than 1 Sv between 2010 and 2011 (see section 3h). Thus, this pattern suggests that the Loop Current penetrated farther north on average during 2011.

The North Brazil Current, which sheds rings that carry waters from the South Atlantic Ocean into the North Atlantic, continued to exhibit anomalous behavior as reported in the *State of the Climate in 2010* report (Fig. 3.20). Sea heights associated with the current and rings continued having the large values observed in 2010; and seven rings were identified to shed. Transport values of this current and its retroflection remained average during 2011.

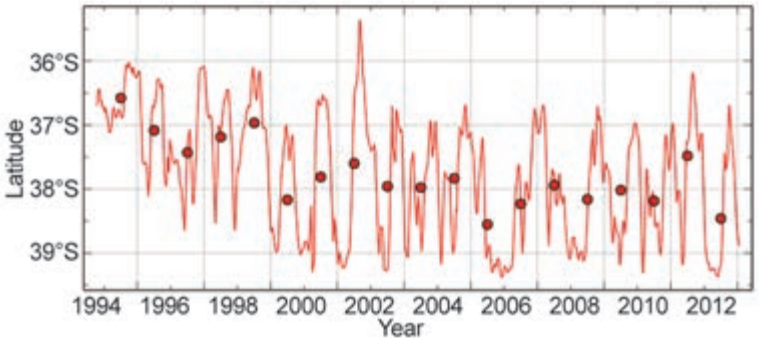

Fig. 3.20. Position of the Brazil-Malvinas front at its separation from the South American continental shelf break, resolved by the change in sea height across the front (http://www.aoml.noaa.gov/phod/altimetry/cvar/mal/BM_ts.php). The solid line is a 28-day running average; dots indicate annual averages.

Against the east coast of South America, the southward-flowing warm, salty Brazil Current meets the northward flowing cold, fresh Malvinas Current to create the Confluence Front. During 2011, the separation of the front from the continental shelf break continued to exhibit annual periodicity driven by wind stress curl variations (cf., Goni and Wainer 2001). The annual mean position of the front in 2011 was 38.5°S, a shift to the south from the 37.5°S position in 2010. This location is as far south as the annually-averaged front has been seen since the launch of the TOPEX/Poseidon altimeter in 1992, and was matched by only one other year (2004). Since 1992, the front has shifted significantly southward in response to wind stress curl changes driven by SST anomalies advected from the Indian Ocean (Lumpkin and Garzoli 2010; Goni et al. 2011).

h. Meridional overturning circulation observations in the subtropical North Atlantic—M. O. Baringer, S. A. Cunningham, C. S. Meinen, S. Garzoli, J. Willis, M. Lankhorst, A. Macdonald, U. Send, W. R. Hobbs, E. Frajka-Williams, T. O. Kanzow, D. Rayner, W. E. Johns, and J. Marotzke

For several years, this section has reported on the meridional redistribution of mass associated with the large-scale vertical circulation within ocean known as the meridional overturning circulation (MOC). Here, the MOC is defined as the maximum of the vertically integrated basin-wide stream function, which changes as a function of latitude and time and is influenced by many physical systems embedded within it. It is related to the meridional transport of heat (MHT) in the oceans, although the relationship may not be direct and can vary with latitude; for example, where horizontal gyre circulation is strong, the heat transport can largely be ascribed to the wind-driven circulation. Variability in oceanic MHT can in turn contribute to heat storage, sea-level rise, and air-sea fluxes and hence influence local climate on land. Therefore, closing the ocean heat budget is a central area of study for understanding and predicting societally-relevant impacts from the oceans. Changes in MOC and MHT can be inferred from "fingerprint" changes in ocean temperature, sea-level rise, and changes in individual current systems (see Baringer et al. 2011 and previous *State of the Climate* reports for more discussion). This annual report focuses on the longest time series observations of ocean heat and mass transport currently available and what can be inferred from them about the current state of the MOC and MHT.

Recommendations for a coordinated observing system to begin to measure MOC were presented at the international conference OceanObs'09 in September 2009 (e.g., Cunningham et al. 2010; Rintoul et al. 2010) and subsequent planning workshops focused on expanding existing observations to include the subpolar North and South Atlantic (e.g., Garzoli et al. 2010). The most complete MOC observing system has been in place since April 2004, and spans the subtropical gyre in the North Atlantic near 26.5°N. The system is composed of UK-NERC RAPID-WATCH moorings, US-NSF Meridional Overturning Circulation Heat-Transport Array (MOCHA), and the US-NOAA Western Boundary Time Series program (see also Rayner et al. 2010; Chidichimo et al. 2010).

The estimates of MOC from the 26.5°N array include data from April 2004 to December 2010 (see also Rayner et al. 2010), shown in Fig. 3.21. Over this

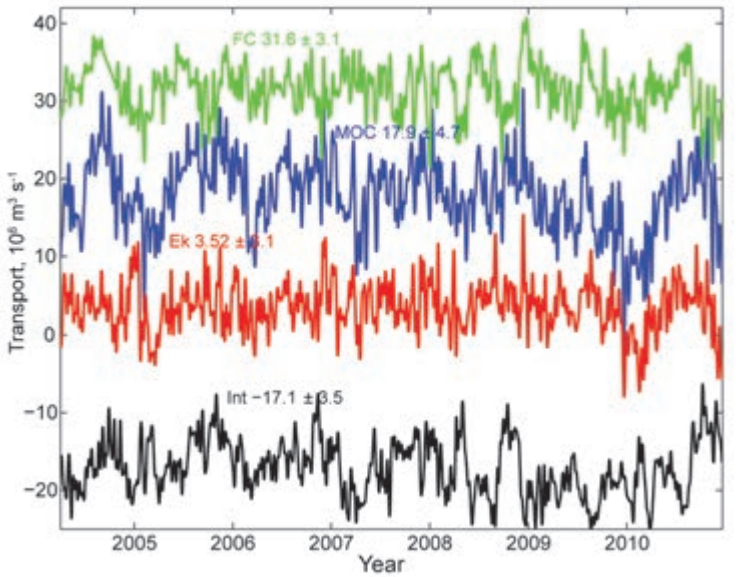

Fig. 3.21. Daily estimates of the strength of the meridional overturning circulation (MOC; blue line) and its components, the Florida Current (FC; green), wind-driven Ekman transport (Ek; red), and the geostrophic interior (Int; black), as measured by the UK National Environmental Research Council Rapid Climate Change Program, the National Science Foundation's Meridional Overturning and Heat transport Array, and the NOAA Western Boundary Time Series Program. The interior volume transport estimate (accurate to 1 Sv, Cunningham et al. 2007) is based on the upper ocean transport from April 2004 to December 2010 (see also Rayner et al. 2010; Kanzow et al. 2010), with a 10-day low pass filter applied to the daily transport values.

time period, the MOC had a mean transport of 18.1 Sv with a high of 31.6 Sv, a low of -2.6 Sv in December 2009 and a standard deviation of 4.7 Sv (using the twice daily values filtered with a 10-day cutoff as described in Cunningham et al. 2007). From early December 2009 through the end of April 2010, the MOC sustained low values with a mean of 9.8 Sv. At the end of the time series in December 2010, the MOC was again relatively low, with a transport of about 13 Sv. These two low MOC "events" were produced by a combination of changes occurring on different time scales (e.g., short-term Ekman and Florida Current transport changes) and long-term changes in the southward geostrophic flow. Overall, the Florida Current and Ekman (EK) transport were about 2 Sv less northward than usual and the southward thermohaline circulation was about 2 Sv stronger, leading to a year-long anomaly of about 5 Sv – 6 Sv in the MOC. With these two events present at the end of the multiyear time series, a linear regression of MOC versus time yields a decrease of -6 ± 0.3 Sv decade^{-1} (95% confidence). A linear trend estimated with the time series ending in December 2009 has a trend of only -4.8 Sv decade^{-1}. Baringer et al. (2011) reported an insignificant trend through April 2009 of -0.8 ± 1.6 Sv decade^{-1}. It is clear that 2010 was an unusual year for MOC transport across 26°N, but given the large variability of MOC estimates, it would be imprudent to ascribe too much to the last year of values in determining a decadal trend. After six years of data, however, a clear seasonal signal is beginning to emerge (Kanzow et al. 2010), with a low MOC in April and a high MOC in October with peak to peak range of 6.9 Sv. The seasonal cycle of the MOC appears to be largely attributable to seasonal variability in the interior rather than Ekman or Florida Current fluctuations; Kanzow et al. (2010) show that the interior seasonal cycle is likely due to seasonal upwelling through a direct wind-driven response off Africa.

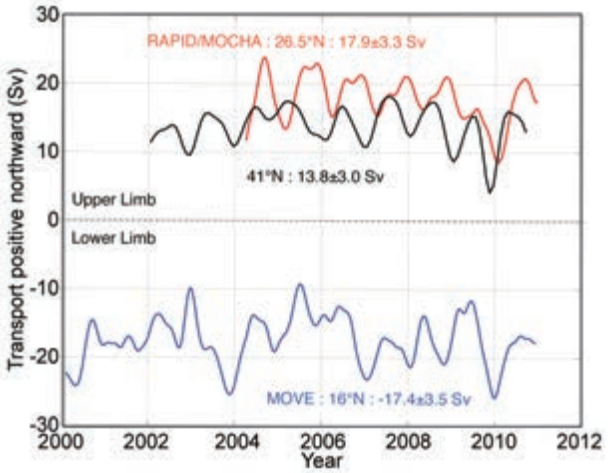

Fig. 3.22. Estimates of the MOC in the Atlantic Ocean from the Argo/Altimetry estimate at 41°N (black; Willis 2010), the Rapid/MOC/MOCHA/WBTS 26°N array (red; Cunningham et al. 2007), and the German/NOAA MOVE array at 16°N (blue; Send et al. 2011) are shown for 2000–12. All time series have a three-month running mean applied.

Two other approaches for estimating Atlantic MOC were developed by Willis and Fu (2008) and Send et al. (2011). Near 41°N, Willis and Fu (2008) used a combination of Argo data and satellite altimetry (measuring sea-surface height fluctuations on 10-day global grid) to determine the absolute geostrophic transports in the upper 2000 m of ocean referenced to subsurface Argo drift velocities. The use of altimetry data, which is well resolved in time, helps to reduce aliasing from the Argo profile data. The MOC time series from 41°N following Willis (2010) is shown in Fig. 3.22 with a three-month running mean applied. The mean value is 13.8 Sv, with similar, slightly smaller variability than found in the 26°N MOC time series (3.0 Sv vs. 3.3 Sv). The decrease in mean MOC strength with increasing latitude is a common feature of observations and models (e.g., Ganachaud and Wunsh 2000; Wuncsh and Heimbach 2009). Willis (2010) reported an insignificant trend in the MOC from 2002 to 2009, consistent with the insignificant trend in the 26°N data to April 2009, before the relatively low transport "event" in late 2009–early 2010. Of note is that the low MOC "event" described earlier in the 26°N data, appears in the 41°N data slightly earlier in time. Both time series have relatively strong annual cycles, slightly shifted in phase. Further examination of the causes of this likely basin-scale "event" and the causes of the shift of seasonal variability is needed.

Since 2000, an array of dynamic height moorings and one current meter mooring have been in place near 16°N to measure the transport fluctuations of the North Atlantic Deep Water (NADW; Kanzow et al. 2008). This NADW time series provides transport estimates of the deepest part of the MOC and has been shown by Kanzow et al. (2008) to be a reasonable index for the strength of the MOC at 16°N for multiannual timescales (e.g., a stronger southward negative flow of NADW corresponds to an increased MOC). The NADW transport time series shows substantial variability (on the order of 3.5 Sv), with a weaker annual cycle than at 26°N or 41°N (Fig. 3.22). There is some suggestion of a decrease in the southward NADW of 20% over the observation period that

would imply a decrease in the MOC (Send et al. 2011). This is consistent with the trend computed from the complete 26°N time series; however, multidecadal fluctuations of the MOC are expected from natural variability and cannot as yet be ascribed to climate change (Send et al. 2011).

Another time series of a major ocean current that contributes to the MOC variability is also the longest open ocean transport time series. Figure 3.23 shows the time series of the Florida Current, which has been measured since 1982 using a submarine cable across the Straits of Florida in combination with regular hydrographic sections Bahamas (e.g., Meinen et al. 2010; Baringer and Larsen 2001). In 2011, the median transport through the Florida Straits was 31.4 ± 1.1 Sv. For the previous four years, the annual average Florida Current transport decreased from 32.1 ± 1.0 Sv in 2007 to 30.7 ± 1.5 Sv in 2010 (error bars represent the standard deviation of daily values divided by the square root of the degrees of freedom calculated for each year where typical decorrelation time scales are about 20 days). The annual mean of 2011, no longer falls within the lowest quartile of mean annual values (long-term median annual average and interquartile range of 31.8 ± 0.5 Sv). Note that while recently the annual means appear to have decreased (April 2004 to December 2010 trend of -1.9 ± 0.2 Sv decade^{-1}, 95% significance), there is only a small significant long-term trend to the Florida Current transport (Fig. 3.23, bottom; trend for complete daily time series is -0.2 ± 0.06 Sv decade^{-1}). The daily fluctuations of Florida Current transport generally fall within 95% confidence levels (32.0 ± 1.0 Sv); the 95% confidence range of daily transport values is shown in Fig. 3.23. There were, however, five extreme low transport events during the year (Fig. 3.23); the most significant events lasting over three days or more occurred during 17–19 July and 30 July–2 August, with values as low as 25.1 Sv. In comparison, there were only three events with transport higher than the 95% confidence range, and no such event lasted for more than a day. Due to the fact that these events were relatively short lived, it is likely they were local responses to atmospheric forcing and coastally-trapped wave processes and are not particularly indicative of a climatically important shift (e.g., Mooers et al. 2005). Nevertheless, these transient fluctuations can have important environmental consequences due to dynamic sea-level changes. For example, it was previously reported that in the summer of 2009, the east coast of the United States experienced a high sea-level event that was unusual due to its unexpected timing, large geographic scope, and coastal flooding that was not associated with any storms (Sweet et al. 2009). Sweet et al. showed that this anomalous event was related to the anomalously low Florida Current transport; a reduced Florida Current transport corresponds to a lower sea-surface height gradient across the front and hence higher sea-level onshore. In 2011, the low transport events could reasonably be inferred to have influenced sea-level along the eastern US; however, as of this report, no relationship has been documented.

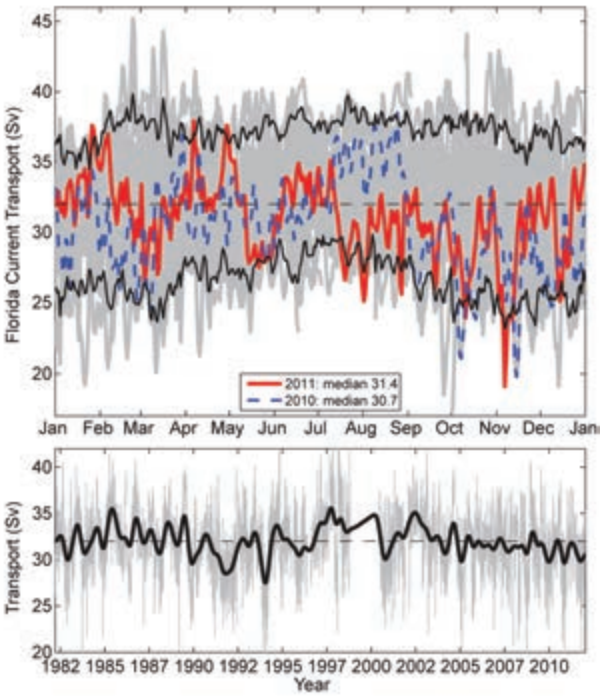

Fig. 3.23. (Top) Daily estimates of the transport of the Florida Current during 2011 (red solid line) compared to 2010 (dashed blue line). The daily values of the Florida Current transport for other years since 1982 are shown in gray and the 95% confidence interval of daily transport values computed from all years is shown in black (solid line); the long-term annual mean is dashed gray. The mean transport in 2011 was 31.4 ± 1.1 Sv, which is less than the long-term mean for the daily values of the Florida Current transport (32.2 Sv). (Bottom) Daily estimates of the Florida Current transport for the full time series record (gray), a smoothed version of transport (heavy black line; using a 30-day running mean six times) and the mean transport for the full record (dashed gray).

In the South Atlantic, a time series of MOC and MHT has been maintained since 2002 (Fig. 3.24), using a high-density expendable-bathythermograph (XBT) line (Garzoli and Baringer 2007; Dong et al. 2009). The mean heat transport across 35°S is 0.55 ± 0.14 PW (petawatt, 1 PW = 10^{15} watts). Following an increase in heat transport since 2008, the year 2011 had a substantial increase in the mean annual

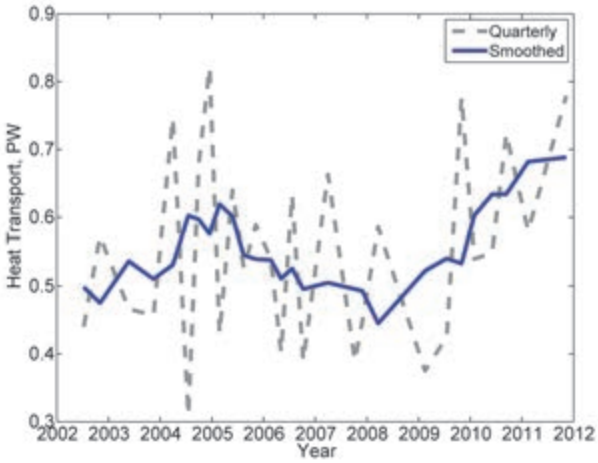

Fig. 3.24. Heat transport in the South Atlantic near 35°S derived from quarterly transects along the high-density line AX18 (gray dashed line) and smoothed values of heat transport (using a five-point running mean; blue solid line). Heat transport values are computed following the methodology of Baringer and Garzoli (2007).

transport value (0.68 PW), the highest recorded annual mean (however, still within one standard error of the mean). According to Dong et al. (2009) the changes in MHT are well correlated with changes in the MOC. This correlation implies an increase in the MOC in the South Atlantic since 2008. The meridional coherence of changes in MOC and heat transport and the relative lead/lag is an active area of research. Heimbach et al. (2011) found that changes in the upper ocean near 35°S could be precursors to changes in the MOC across 26°N as early as four years into the future.

i. Sea level variability and change—

M. A. Merrifield, P. Thompson, D. P. Chambers, G. T. Mitchum, M. Menéndez, R. S. Nerem, E. Leuliette, L. Miller, S. Holgate, J. J. Marra, and W. Sweet

Sea level is a primary indicator of climate variability and change over a wide range of time and space scales. Global mean sea level provides a measure of volume changes associated with ocean heat content changes and water mass exchange with the land. Regional sea level variations reflect changes in the wind-forced circulation and transports of heat and salt. Extreme sea levels reflect storm patterns and their variation from year to year, as well as sea level extremes associated with ENSO and other climate modes of variability. Not only is sea level change a key climate indicator, it is also potentially one of the more important impacts of climate change.

Sea level variability during 2011 is characterized by first examining seasonal anomalies (Fig. 3.25), which highlight changes associated with variable winds and climate modes of variability. Annual mean sea level deviations and changes from the previous year are considered (Fig. 3.26), and global mean sea level is shown to have been significantly below the long-term trend during 2011 (Fig. 3.27), but is trending sharply back upwards late in the year. Ongoing assessments of the sea level budget are reviewed (Fig. 3.28) to provide context for the 2011 sea level drop in terms of the La Niña conditions that dominated the year. Lastly, extreme sea level conditions during 2011 are characterized based on 30-plus-year tide gauge records (Fig. 3.29). Data for this assessment were obtained from the multimission gridded sea surface height (SSH) altimeter product produced by Ssalto/Duacs and distributed by AVISO, with support from CNES (http://www.aviso.oceanobs.com), and from the University of Hawaii Sea Level Center (http://uhslc.soest.hawaii.edu/), with support from the NOAA Climate Observations Division.

The regional sea level patterns (Fig. 3.25) show that La Niña conditions prevailed during 2011. The La Niña event peaked during the winter of 2010/11

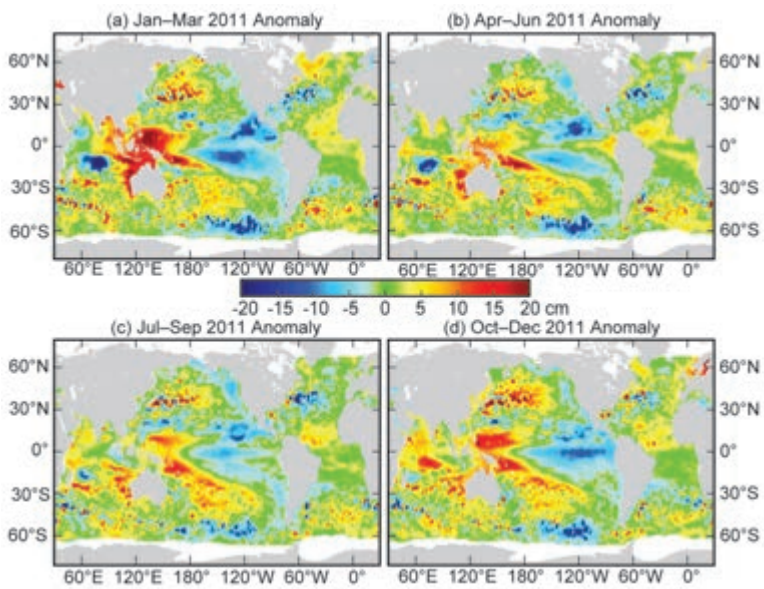

Fig. 3.25. Seasonal SSH anomalies (cm) for 2011 relative to the 1993–2011 base period are obtained using the multimission gridded sea surface height altimeter product produced by Ssalto/Duacs and distributed by AVISO, with support from CNES (http://www.aviso.oceanobs.com).

with high sea levels in the western tropical Pacific and low values in the eastern tropical Pacific (Fig. 3.25a). The stronger trade winds associated with La Niña weakened during the middle of 2011 (see Fig. 3.10), causing a reduction of the zonal sea level gradient and the buildup of positive anomalies in the equatorial Pacific off South America (Fig. 3.25b). As the trades picked up again during the second half of 2011, Pacific sea level anomalies ended the year with an enhanced La Niña state (Fig. 3.25d), although not as strong as the first quarter of the year (Fig.3.25a). Sea levels in the eastern Indian Ocean were positive throughout the year, with a peak in the first quarter. A westward propagating negative anomaly in the central Indian Ocean was evident south of the equator, which was followed by a positive anomaly in the last quarter of the year.

In the Atlantic, the continuation of the negative North Atlantic Oscillation (NAO) index into January was reflected in a negative anomaly in the Baltic (Fig. 3.25a). The index then turned strongly positive for most of the year, excluding the months of June, July, and August. The strongly positive index at the end of 2011 is reflected in the negative Mediterranean anomalies and a reversal to positive anomalies in the Baltic (Fig. 3.25d).

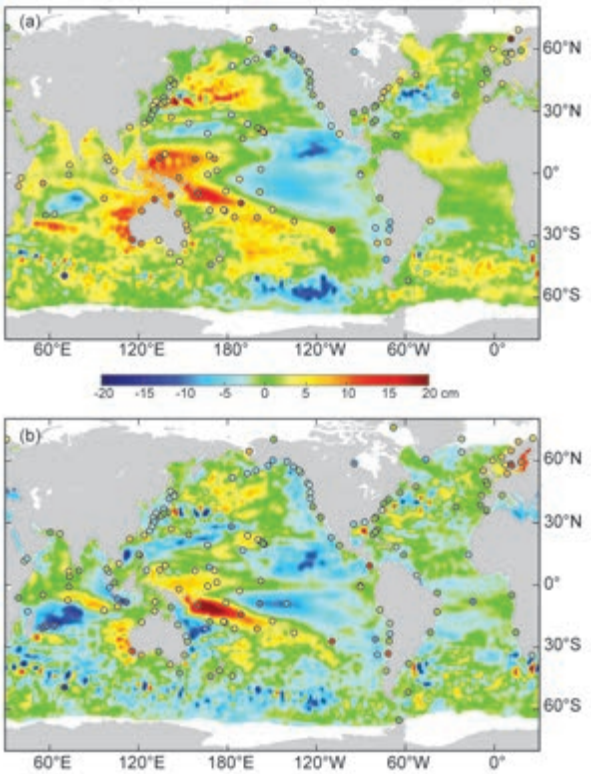

Fig. 3.26. (a) The 2011 SSH anomaly (Ssalto/Duacs product with anomaly, cm) from the 1993–2011 base period is compared to the 2011 anomaly computed for tide gauge data (dots) obtained from the University of Hawaii Sea Level Center (http://uhslc.soest.hawaii.edu/). (b) The difference between 2011 and 2010 annual means (cm).

Annually-averaged sea level during 2011 was dominated by a La Niña pattern across the Pacific and Indian Oceans (Fig. 3.26a). In the North Pacific, anomalous winds in the Aleutian Low region exhibited a negative wind stress curl (see Fig. 3.10), which contributed to high sea levels in the central Pacific and low sea levels along the western coast of North America. This wind and sea level pattern is typical of the negative phase of the Pacific decadal oscillation (PDO; Mantua et al. 1997; Cummins et al. 2005), which is consistent with the negative values of the PDO index since mid-2010. Over the Southern Ocean, wind stress curl changes in the region of strong westerlies accompanied a broad negative sea level anomaly west of the southern tip of South America (Fig. 3.26a). Annual sea levels were generally high in the tropical Indian Ocean, with the exception of the strong negative anomaly in the eastern Indian Ocean mentioned previously. Sea level deviations in the Atlantic Ocean showed bands of relatively high sea level in the South Atlantic just north of the equator, and in the subpolar North Atlantic.

The sea level tendency for 2011, measured as the difference between the 2011 and 2010 annual means, shows weak to negative changes over broad regions of the ocean (Fig. 3.26b). Positive changes were most evident in the South Pacific convergence zone (SPCZ), off the west coast of Australia, and in the central North Pacific (Fig. 3.26b). The changes in the tropical Pacific suggest a tendency for stronger trades in 2011 relative to 2010, and a net strengthening of La Niña conditions. In general, enhanced rates of sea-level rise have been observed in the western tropical Pacific for at least the past two decades (Merrifield 2011; Becker et al. 2012). These changes appear to be associated with a multidecadal enhancement of the trade winds in the Pacific (Merrifield and Maltrud 2011). Negative sea level changes were most evident in the Southern Ocean, the Indian Ocean south of the equator, and the off-equatorial regions in the eastern Pacific. Annual sea level changes in the Atlantic were relatively weak compared to the other ocean basins, but Baltic sea levels showed a large increase relative to 2010 while the Mediterranean showed a decrease (Fig. 3.26b). These changes are associated with a NAO index that showed the most positive value since 1994 in 2011, as compared to the most negative value on record in 2010.

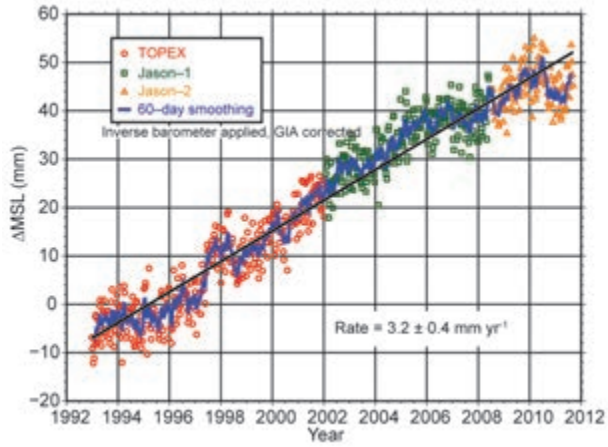

Fig. 3.27. Time series of global mean sea level (mm) since 1993 from the TOPEX and Jason series of satellite radar altimeters. Seasonal signals have been removed from the data and inverse barometer and global isostatic adjustment corrections have been applied (see Nerem et al. 2010).

The average global rate of sea level change computed over the years 1993–2011 is 3.2 ± 0.4 mm yr^{-1} (Fig. 3.27; Beckley et al. 2010; Leuliette and Scharroo 2010; Nerem et al. 2010). Relative to the long-term trend, global sea level dropped noticeably in mid-2010 and reached a local minimum in 2011. The drop has been linked to the strong La Niña conditions that have prevailed throughout 2010–11 (section 3b). Global sea level increased sharply during the second half of 2011.

The relative contributions to the total sea level changes from addition of mass and density changes has been measured since 2005 when global upper ocean temperature and salinity observations from the Argo float array and ocean mass variations from the Gravity Recovery and Climate Experiment (GRACE) became available (Leuliette and Willis 2010; Llovel et al. 2009). The observations show (Fig. 3.28a) that the sea level budget since 2005 can be closed to within the range of uncertainties over a variety of time scales. Although the contribution of deep ocean heat content to the long-term trend in sea level deserves attention, for now this contribution appears to be smaller than the uncertainty. Over this brief time period and for latitudes between ± 66° where altimetry observations are available, the mean rate of total sea level rise is 1.4 ± 0.4 mm yr^{-1} (1 standard error; Leuliette and Willis 2010). This rate computed with the data since 2005 is not comparable to the longer-term rate from 1993 since at least 10 years of data are required to determine a reliable long-term rate (Nerem et al. 1999). This rate is, however, in agreement (Fig. 3.28a) with the sum (1.3 ± 0.4 mm yr^{-1}) of the rates of the upper ocean steric (0.2 ± 0.2 mm yr^{-1}) and ocean mass components (1.2 ± 0.3 mm yr^{-1}) (Fig. 3.28b).

This sea level budget material is based on a short record, but shows proximity to the ability to understand total sea level changes measured by altimetry and tide gauges in terms of ocean density and mass changes. In addition, these contributions can be understood both in terms of buoyancy and mass inputs as well as redistributions of each quantity. In future years, such analyses will be of central importance in this annual review.

Extreme sea level events are measured in daily tide gauge records. The highest sea level events are primarily caused by a combination of storm surges associated with midlatitude and tropical storms and tidal fluctuations, but other factors such as mean sea level variation can contribute to extreme sea level values. The daily averages considered here exclude the semidiurnal and diurnal tidal contributions to

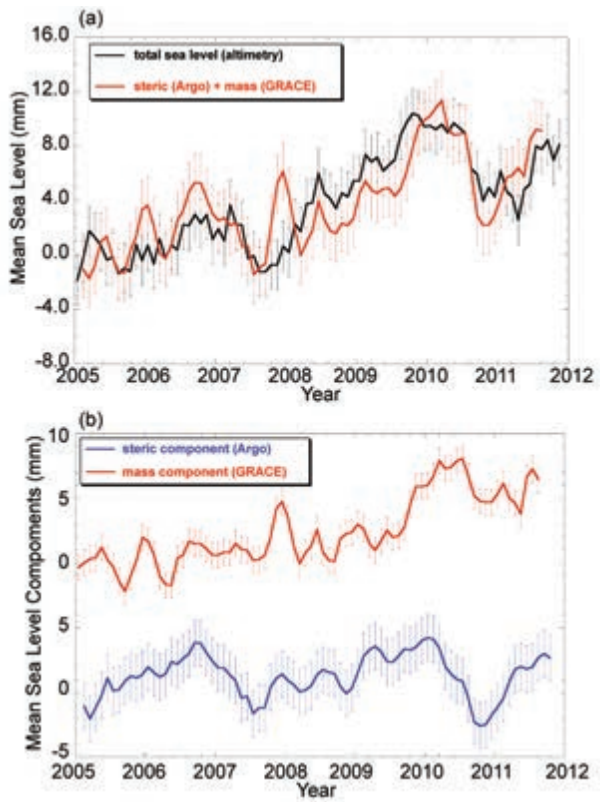

Fig. 3.28. Monthly estimates (in mm) from (a) Jason-1 and Jason-2 of global mean sea level (black), which are in general agreement with the sum of the steric component from Argo and ocean mass component from GRACE (red), and (b) the individual components (in mm) as measured by GRACE (red) and Argo (blue). Seasonal signals were removed and the time series were smoothed with a three-month running mean. Error bars represent one standard error.

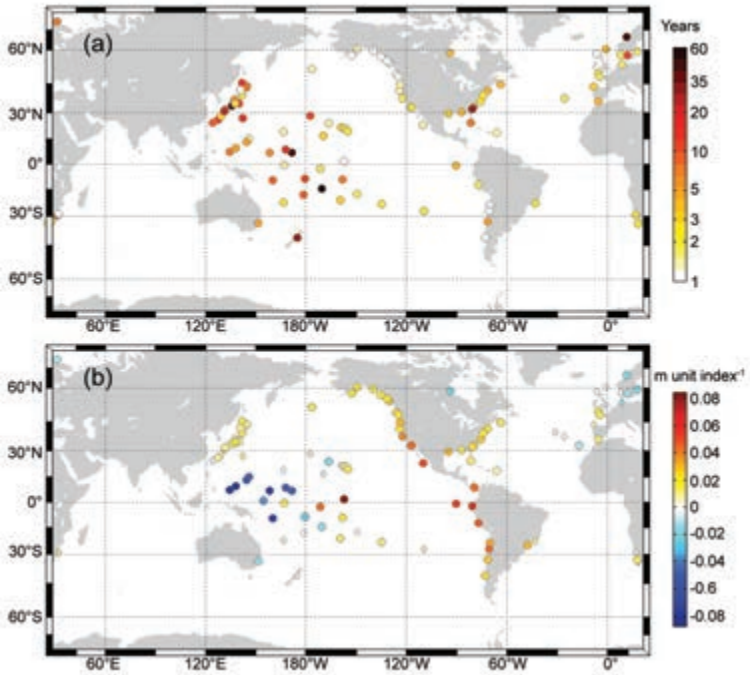

Fig. 3.29. (a) Return period/averaged recurrence interval (years) associated with the highest sea level event during 2011 at each station. (b) Influence of Niño 3.4 index on extreme sea levels (m unit index^{-1}).

extreme levels. An estimation of the return period associated with the measured annual maxima of daily averaged sea level for 2011 provides a means of comparing last year's extremes with previous years (Fig. 3.29a). The return periods are estimated from the empirical distribution function of the annual maxima for each tide gauge record. The more unusual sea level extremes during 2011 were in the SPCZ region, along the coast of Florida, and in parts of the coast of the Scandinavian countries in northern Europe. Extreme events along the west coast of North America and Europe were unremarkable. The extremes in the western Pacific were consistent with the strengthening of La Niña conditions during 2011, whereas the higher extreme values in northeast Europe were coincident with the positive phase of the Arctic Oscillation (a close relative of the NAO) during the 2011 winter, which drives ocean storms farther north. The larger values obtained along the Florida coast are associated with the passage of a strong nontropical storm.

Interannual fluctuations in extreme sea levels can depend on regional climate patterns. To investigate the climate variability in extreme sea levels, a nonstationary extreme value analysis has been applied to the monthly maxima of daily-averaged tide gauge records, following Menéndez and Woodworth (2010). The statistical relationship of ENSO in extreme sea levels is studied by adding the linear covariate (Niño 3.4 climate index) in the location parameter of the generalized extreme value (GEV) distribution. Although a higher influence of ENSO is expected across the tropical Pacific, the sensitivity of extreme sea levels to ENSO has a worldwide effect (Fig. 3.29b). A negative value of the Niño 3.4 index characterizes a La Niña event, hence the negative values in Fig. 3.29b correspond to a positive extreme sea level change during La Niña, and positive values correspond to negative extreme sea level change. The higher return periods in the western tropical Pacific and low values along the eastern Pacific (Fig. 3.29a) are generally consistent with La Niña conditions.

j. Global ocean carbon cycle—C. L. Sabine, R. A. Feely, R. Wanninkhof, T. Takahashi, S. Khatiwala, and G.-H. Park

1) Air-sea carbon dioxide fluxes

Although independent estimates of decadal-scale ocean carbon uptake agree within their uncertainty (Gruber et al. 2009), data-based studies suggest regional, year-to-year variations in oceanic carbon dioxide (CO_2) uptake (Doney et al. 2009). These studies underscore the need for global, long-term observations of the surface ocean carbon cycle and for systematic handling of such data to secure their long-term accessibility. The number of annual surface CO_2 observations has been growing exponentially since the 1960s such that today well over one million observations are reported to data centers each year. In 2011, a new product called the Surface Ocean CO_2 Atlas (SOCAT) was released. SOCAT contains 6.3 million surface water CO_2 measurements from more than 1850 voyages in the global oceans and coastal seas between 1968 and 2007. Two SOCAT products are publicly available: (1) a global dataset of recalculated surface ocean fCO_2 (fugacity of CO_2, similar to partial pressure) in a uniform format which have been subject to data quality control; and (2) a global, gridded monthly mean surface water fCO_2 data product with minimal temporal and spatial interpolation (http://www.socat.info). The SOCAT products are intended to complement the LDEO database, which contains much of the same data but was processed with different quality control procedures. The latest release of the LDEO database includes 3.7 million data points from 1957 to 2010 (Takahashi et al. 2011).

The LDEO database is used to generate the LDEO CO_2 climatology, which provides the monthly patterns of air-sea CO_2 fluxes during a "normal" non-El Niño year taken to be 2000 (Takahashi et al. 2009). The annual mean for the 2000 net CO_2 uptake flux over the global oceans is estimated to be 1.4 ± 0.7 Pg (10^{15}g) C yr^{-1}. The equatorial Pacific (14°N–14°S) is the major source for atmospheric CO_2, emitting about 0.48 Pg C yr^{-1}, and the temperate oceans between 14° and 50° in the both hemispheres are the major sink zones with an uptake flux of 0.70 Pg C yr^{-1} for the northern zone and 1.05 Pg C yr^{-1} for the southern zone. The uncertainty in the gas exchange rate is estimated at ± 30%, and hence the estimated sea-air CO_2 flux climatology is uncertain to at least this magnitude. Improvements in wind speed products and parameterization of gas exchange rate are needed for a reduction of the uncertainty in CO_2 flux estimates.

The seasonal and interannual variability in CO_2 fluxes for the last three decades is estimated using the algorithms of Park et al. (2010). Due to lags in availability of quality-controlled data streams, the surface air-sea CO_2 fluxes reported in the *State of the Climate* reports are a year behind. The global net uptake CO_2 flux for the 2010 transition period from El Niño to La Niña was estimated to be 1.30 Pg C yr^{-1}, lower than the 1982–2010 long-term mean of 1.47 Pg C yr^{-1}. The smaller CO_2 effluxes in the equatorial Pacific during the first four months of the El Niño period partially compensate CO_2 effluxes in the remaining months during the La Niña (Fig. 3.30). During the El Niño period, the central equatorial Pacific shows less CO_2 outgassing compared to the 29-year mean values (Fig. 3.30b). This flux anomaly pattern is a result of the El Niño Modoki, showing greater SST anomalies in the central equatorial Pacific than in the eastern equatorial Pacific (Ashok et al. 2007). However, despite the El Nino conditions at the start of 2010, the equatorial Pacific still showed high CO_2 effluxes. Effluxes of CO_2 for both the El Niño and La Niña periods in the eastern equatorial Pacific are higher than the 29-year average (Fig. 3.30b,c). These high CO_2 effluxes are attributed to intensified upwelling of deep water rich in CO_2 caused by an increase of wind speed observed for 2010.

Compared to long-term averages, higher CO_2 uptake is found in the high latitudes of the northern and southern Atlantic Ocean, and higher CO_2 effluxes and less CO_2 uptakes are observed in the high southern Pacific Ocean. Negative CO_2 flux anomalies (blue colors in Fig. 3.30a) found in the high-latitude Atlantic Ocean are predominantly caused by SST anomalies in the regions. For the high southern Pacific Ocean, the positive CO_2 flux anomalies (red colors in Fig. 3.30a) are caused primarily by SST anomalies and partially reinforced by wind speed anomalies. The monthly flux maps and anomalies from 1982 to 2010 can be obtained from http://cwcgom.aoml.noaa.gov/erddap/griddap/aomlcarbonfluxes.graph.

During 2011 a comprehensive comparison of model-based and data-based estimates of sea-air CO_2 fluxes and trends over the past two decades was performed.

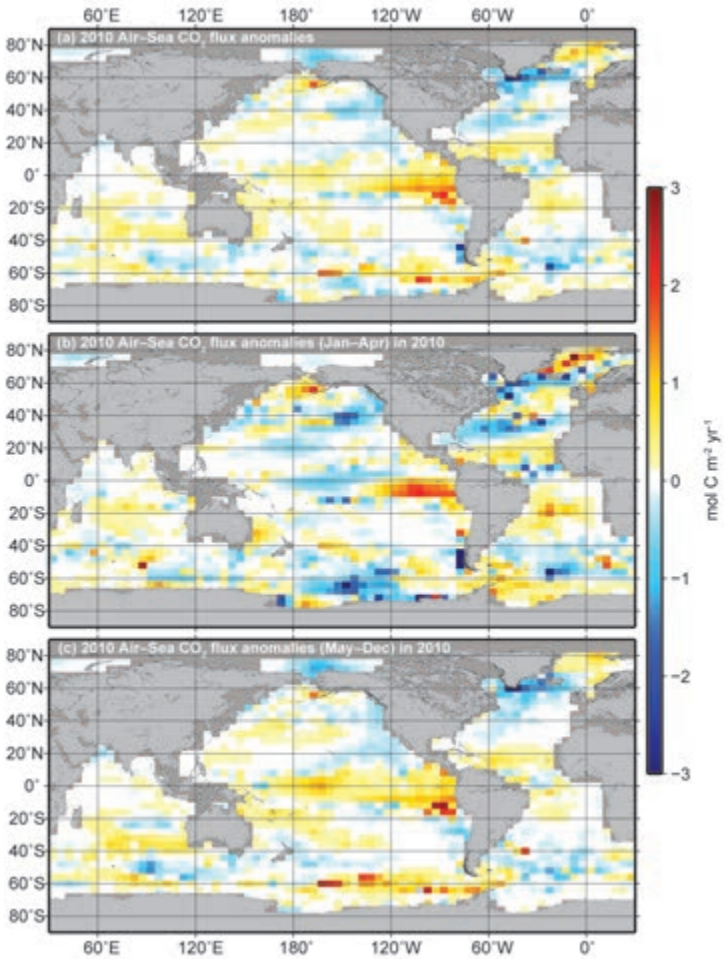

Fig. 3.30. Global distributions of air-sea CO_2 flux anomalies (mol C m^{-2} yr^{-1}) for (a) 2010, (b) Jan–Apr, and (c) May–Dec, compared to the 1982–2010 mean values for the corresponding months as calculated from the Park et al. (2010) approach. Positive values indicate less uptake or more release of CO_2 by the ocean.

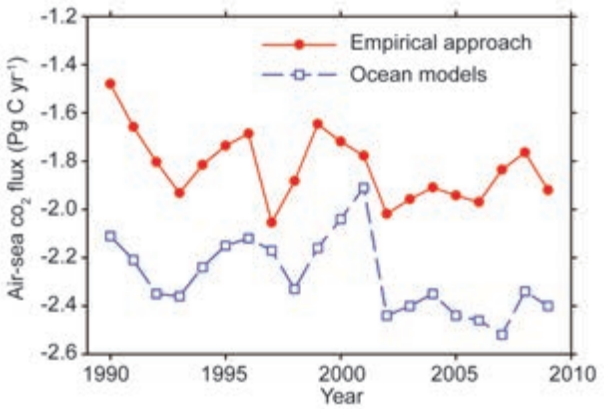

Fig. 3.31. Comparison of anthropogenic air-sea CO_2 fluxes (Pg C yr^{-1}) based on a composite of ocean models (blue line with squares) and an empirical data–based approach (red line with circles). For the comparison, CO_2 fluxes caused by atmospheric CO_2 increase, the riverine CO_2 flux (0.45 Pg C yr^{-1}), and undersampling error of observations (0.2 Pg C yr^{-1}) are added to the net air-sea CO_2 fluxes derived in the Park et al. (2010) approach. The CO_2 fluxes from the empirical approach, here, were calculated using the cross-calibrated multiplatform (CCMP) wind speeds (Atlas et al. 2011).

There is good agreement of increasing uptake trends of about 0.12 Pg C decade^{-1} with significant interannual variability driven by large-scale climate reorganizations such as ENSO. However, there are appreciable offsets in the absolute magnitudes. The empirical approach, numerical ocean biogeochemistry models such as those from the National Center for Atmospheric Research (NCAR), and atmospheric inverse models all show anthropogenic CO_2 uptake of 1.4 Pg C yr^{-1} – 2.0 Pg C yr^{-1}. In contrast, global constraints and models adjusted to global constraints, such as the University of East Anglia (UEA) model runs, show uptakes ranging from 1.9 Pg C yr^{-1} to 2.5 Pg C yr^{-1} (Fig. 3.31). The differences may be related to the carbon cycle representation in the model, but they may also be related to differences in the physical forcing in the models. The various wind products are improving. Since 98% of the ocean area has fairly low wind speeds in the 4 m s^{-1} – 11 m s^{-1} range where the different wind products generally agree, this is not a huge problem for most areas. However, there are still issues in certain key regions (e.g., Southern Ocean and coastal regions) with the available wind products. The use of different wind products and different exchange coefficients in publications makes it challenging to objectively compare results. Moreover, reanalyses products are continually updated and version and source of the wind product used should be specified. For example, the global CO_2 fluxes calculated using the pCO_2 climatology normalized to year 2000 and two different wind products, NCEP Reanalysis II and CCMP, are 1.4 Pg C yr^{-1} and 1.2 Pg C yr^{-1}, respectively, despite normalization of parameterization of gas transfer and wind speed for the different global mean winds of the products. This is caused by systematic large-scale differences in the two products with the NCEP II product showing lower winds in the equatorial band and higher winds at higher latitudes. The CO_2 fluxes estimated from NCEP winds show less CO_2 effluxes in the equatorial Pacific and greater CO_2 uptake in the subtropic and northern areas than from CCMP winds, and therefore show a greater net uptake.

2) Subsurface carbon inventory

The U.S. CLIVAR/CO_2 Repeat Hydrography Program has spent the last decade reoccupying 19 hydrographic sections initially sampled in the 1990s as part of the World Ocean Circulation Experiment (WOCE) hydrographic survey. These reoccupations provide information on how ocean carbon and other physical and biogeochemical tracers are changing over time (http://ushydro.ucsd.edu /). Between Febru-

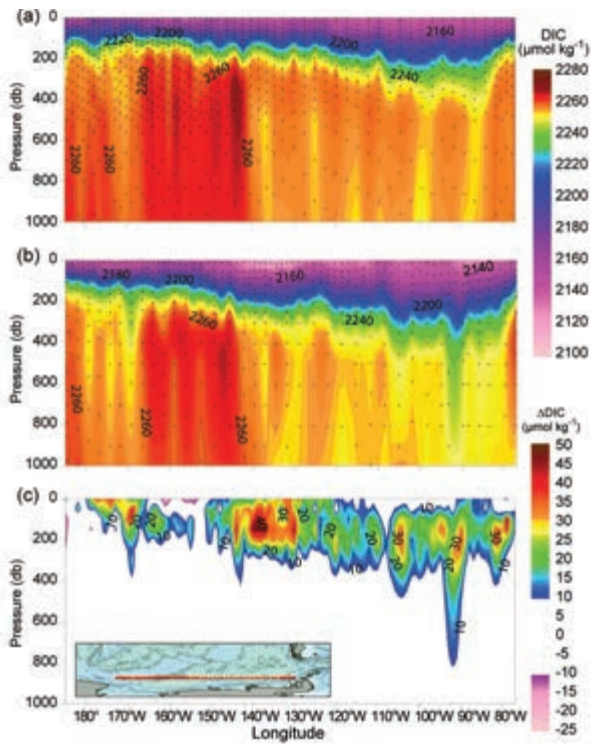

Fig. 3.32. Sections of dissolved inorganic carbon across the Pacific sector of the Southern Ocean (S4P) in (a) Feb–Apr 2011, (b) Feb–Mar 1992, and (c) the 2011 minus 1992 difference (µmol kg^{-1}). The 1992 data are from Chipman et al. (1997).

ary and April 2011, an east-west cruise line (S4P) in the South Pacific, nominally along 67°S, was occupied as a repeat of a similar cruise run between February and March 1992. Figure 3.32 shows the observed dissolved inorganic carbon (DIC) distributions from each of these cruises. The bottom panel on Fig. 3.32 shows the estimated DIC increases over the 19-year interval, which varies from no change below 800 m to values greater than 40 μmol kg^{-1} at approximately 200 m depth near 138°W. The main concentration increases are between the surface and 300 m, as expected from an uptake of atmospheric CO_2. The lack of observable changes in the initial analysis of the deep ocean is consistent with previous observations that any changes in deep ocean carbon in the Pacific sector of the Southern Ocean are below reliable detection limits (Sabine et al. 2008). Additional analyses are being conducted to improve the techniques for isolating the anthropogenic component of the DIC concentrations.

While repeat hydrographic measurements are critical for documenting regional changes in the uptake and storage of anthropogenic CO_2, on a global scale, inverse methods have been instrumental in mapping out spatial variations. Figure 3.33a shows one such global estimate of the storage rate of anthropogenic CO_2 for 2010 based on a Green's function method utilizing transient tracers (Khatiwala et al. 2009, 2012, manuscript submitted to *Biogeosciences*). The map shows the largest storage rate is in the North Atlantic associated with the transport of anthropogenic CO_2 into the ocean interior associated with the formation of North Atlantic Deep Water and Labrador Sea Water. High storage rates are also seen at 40°S–50°S associated with the subtropical convergence, another area where intermediate and mode waters are formed and move CO_2 into the ocean interior.

On a global scale, the 2010 open ocean inventory of anthropogenic CO_2 is estimated using Green's function method to be 151 ± 26 Pg C (Khatiwala et al. 2009, 2012, manuscript submitted to *Biogeosciences*). This estimate is based on the GLODAP database of hydrographic and biogeochemical observations (Key et al. 2004) and does not cover the coastal and marginal seas. Estimates for the latter have been recently compiled and updated to 2010 by Khatiwala et al. (2012, manuscript submitted to *Biogeosciences*) and are as follows: Arctic Ocean, 2.7 Pg C – 3.5 Pg C (Tanhua et al. 2009); Nordic Seas, 1.0 Pg C – 1.6 Pg C (Olsen et al. 2010); Mediterranean Sea, 1.6 Pg C – 2.5 Pg C (Schneider et al. 2010); and the East Sea/Sea of Japan, 0.40 ± 0.06 Pg C (Park et al. 2006). This gives a total ocean inventory of approximately 160 Pg C for 2010.

In the Pacific, both inverse methods and repeat hydrography estimates are in reasonable agreement. Both methods show higher storage in the South Pacific compared with the North Pacific (Murata et al. 2007; Sabine et al. 2008), and higher rates in the western North Pacific compared with the eastern basin (Sabine et al. 2008). In other regions, however, the methods do not agree. For example, inverse estimates show higher storage in the North Atlantic relative to the South Atlantic, opposite of the pattern found by studies based on repeat hydrography (Wanninkhof et al. 2010), possibly due to temporal variability not accounted for by the former (Khatiwala et al. 2012, manuscript submitted to *Biogeosciences*).

With the exponential growth of atmospheric CO_2 in the atmosphere, the global rate of annual anthropogenic CO_2 storage is increasing dramatically with time (Fig. 3.33b). Based on a Green's function estimates, the annual storage rate has doubled since the 1970s. As discussed in the previous section, different methods vary in the estimated current uptake

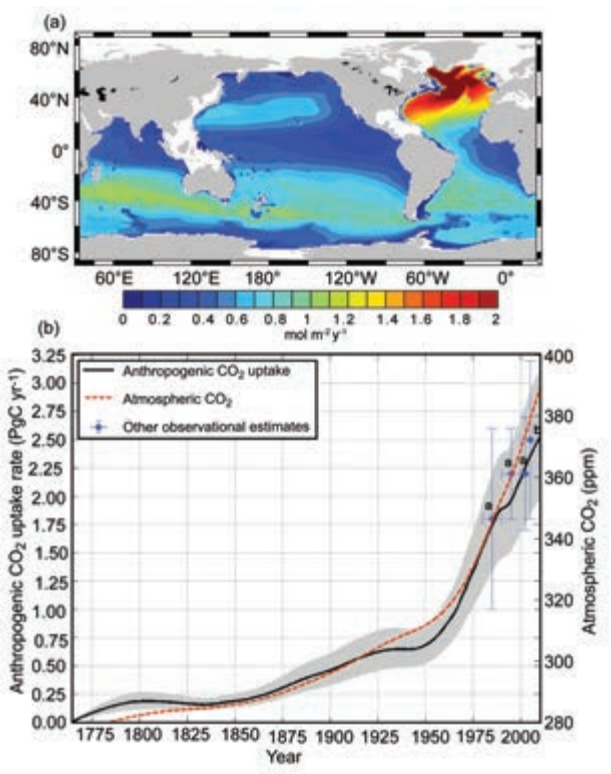

Fig. 3.33. (a) Map of the 2010 annual change in anthropogenic CO_2 column inventory (mol m^{-2} yr^{-1}). (b) Time history of the global ocean anthropogenic CO_2 uptake rate (Pg C yr^{-1}) based on the Green's Function approach of Khatiwala et al. (2009, 2012, manuscript submitted to *Biogeosciences*).

and storage rate, but these differences are within the stated uncertainties. As long as atmospheric CO_2 continues to increase, the oceans will continue to store anthropogenic carbon.

Based on a recent compilation of emissions by Andres et al. (2012, manuscript submitted to *Biogeosciences*), the ocean inventory represents ~43% of fossil fuel and ~29% of total (fossil fuel and land use changes) anthropogenic CO_2 emissions over the industrial period. This is consistent with the earlier work of Sabine et al. (2004) who found that the ocean inventory accounted for nearly half of the fossil fuel CO_2 emitted since the preindustrial era. It should be noted that these values are based on the total accumulation of CO_2 in the ocean since the preindustrial era. If, as in some recent publications (e.g., Le Quéré et al. 2009), the computation is carried out on the basis of the annual rate of CO_2 uptake, which varies significantly with time (Fig. 3.33b), rather different values would be obtained. Thus, at a current ocean uptake rate of 2.5 Pg C yr^{-1} (Khatiwala et al. 2009) and fossil fuel and total emission rates of ~8.5 Pg C yr^{-1} and ~10 Pg C yr^{-1}, respectively, (Solomon et al. 2007; Andres et al. 2012, manuscript submitted to *Biogeosciences*; Carbon Dioxide Information Analysis Center), values of 1/3 and 1/4 of emissions are arrived at for the ocean sink. This highlights the importance of clearly stating the assumptions and qualifications when making statements concerning the efficiency of the ocean sink.

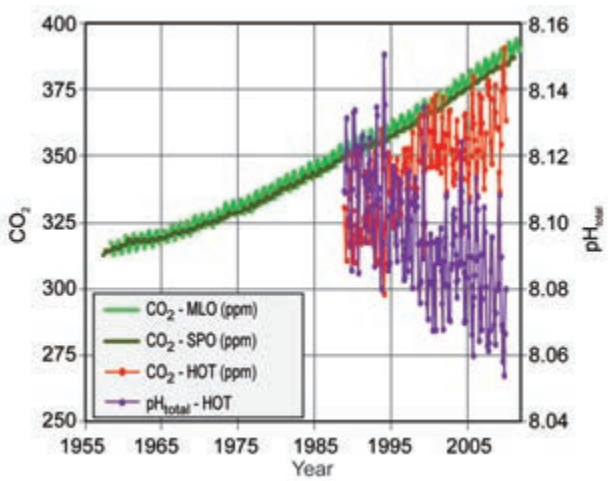

Fig. 3.34. Time series of atmospheric CO_2 (ppm) at Mauna Loa (MLO) and the South Pole (SPO) and surface ocean pH and pCO_2 (µatm) at Ocean Station Aloha (HOT) in the subtropical North Pacific Ocean. [Source: Mauna Loa data: Dr. Pieter Tans, NOAA/ESRL (http://www.esrl.noaa.gov/gmd/ccgg/trends); HOTS/Aloha data: Dr. Matthew Church, University of Hawaii (http://hahana.soest.hawaii.edu)].

3) Ocean acidification

The ocean absorption of CO_2 from the atmosphere has reduced the accumulation of greenhouse gases in the atmosphere, thus slowing the rate of climate change (Solomon et al. 2007). However, when CO_2 enters the ocean it reacts with water to form carbonic acid and its dissociation products. This CO_2 increases ocean acidity and decreases ocean pH in a process commonly referred to as "ocean acidification" (Caldeira and Wickett 2003). The addition of CO_2 to the ocean causes a decrease in carbonate ions, thus lowering calcium carbonate saturation states, making it more difficult for organisms to produce calcium carbonate shells or skeletons (Fabry et al. 2008; Guinotte and Fabry 2008). Since the beginning of the industrial era, the pH of open-ocean surface waters has decreased by about 0.1 pH units, equivalent to an overall increase of ~30% in the hydrogen ion concentration. For example, over the past twenty years atmospheric and oceanic CO_2 near Hawaii have increased by approximately 40 ppm and 40 µatm, respectively, while the pH of those same surface waters have decreased by about 0.04 units (Fig. 3.34).

Recent models have suggested that undersaturated waters, that is, waters with carbonate ion concentrations low enough to dissolve calcium carbonate shells, would shoal to depths affecting western US shelf ecosystems, home to

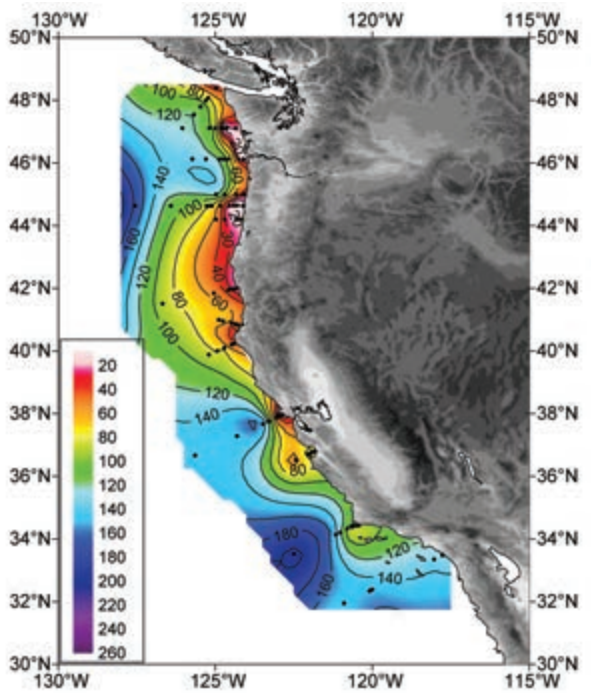

Fig. 3.35. Depth distribution of corrosive undersaturated water (Ωarag < 1.0, pH < 7.75) along western North American continental margin in Aug–Sep 2011. The undersaturated waters are the direct result of the combined impacts of acidification, upwelling, and hypoxic conditions on the continental shelf.

rich fisheries and diverse communities, over the next several decades to a century (Orr et al. 2005; Hauri et al. 2009). However, in 2007, the first detailed observations of carbon chemistry in this region revealed that anthropogenically-acidified waters, undersaturated in aragonite, were already upwelling onto the continental shelf to depths of 40 m – 120 m in most areas and all the way to the surface along a transect in northern California (Feely et al. 2008). Figure 3.35 shows the depth distribution of the undersaturated waters along the continental shelf from a recent cruise in August–September 2011. The undersaturated waters reach depths as shallow as 20 m–30 m off the Washington, Oregon, and northern California coasts.

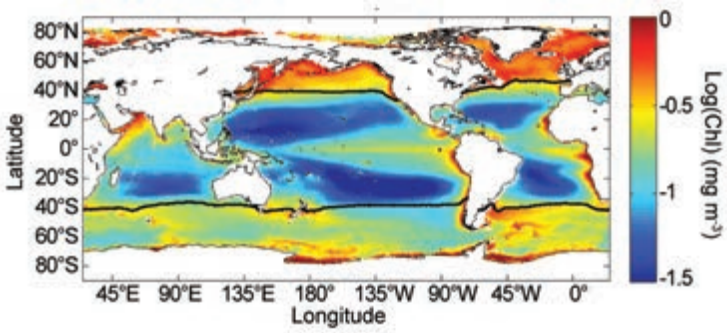

Fig. 3.36. Mean Chl distribution calculated over the entire SeaWiFS record from monthly level 3 imagery (1 Nov 1997–30 Nov 2010) in units of log(mg Chl m^{-3}). Also shown is the location of the mean 15°C SST isotherm (black line).

One area of new research in ocean acidification is linking ocean acidification with low oxygen (hypoxic) events along the continental shelves. Oxygen-poor environments present physiological challenges for marine organisms and these are also expected to increase in prevalence under anthropogenic climate change as a result of surface ocean warming and increased stratification (Bopp et al. 2002; Matear and Hirst 2003; Stramma et al. 2008; Rykaczewski and Dunne 2010). The term "hypoxia" implies levels of oxygenation under which macrofauna are negatively impacted. Conditions ranging from hypoxic (< 65 μM) to anoxic (0 μM) have been observed in near-bottom waters on the inner continental shelf within the California Current System with an apparent increase in the frequency and intensity of the oxygen deficit since 2000 (Chan et al. 2008; Grantham et al. 2004; Hales et al. 2006). The conditions of corrosivity and hypoxia are linked on a process level because when remineralization of organic matter occurs under oxic conditions, oxygen is consumed approximately in stoichiometric equivalence (170:117) with the production of CO_2. Processes that create aquatic oxygen deficits can also exacerbate the formation of corrosive conditions for calcareous organisms. Thus, globally there may be connections between regional hypoxia and ocean acidification on a global scale.

4) Global ocean phytoplankton—D. A. Siegel, D. Antoine, M. J. Behrenfeld, O. H. Fanton d'Andon, E. Fields, B. A. Franz, P. Goryl, S. Maritorena, C. R. McClain, M. Wang, and J. A. Yoder

Phytoplankton photosynthesis in the sunlit upper layer of the global ocean is the overwhelmingly dominant source of organic matter that fuels marine ecosystems. Phytoplankton contribute roughly half of the global (land and ocean) net primary production (NPP; gross photosynthesis minus plant respiration) and phytoplankton carbon fixation is the primary conduit through which atmospheric CO_2 concentrations interact with the ocean's carbon cycle. Phytoplankton productivity depends on the availability of sunlight, macronutrients (e.g., nitrogen, phosphorous), and micronutrients (e.g., iron), and thus is sensitive to climate-driven changes in the delivery of these resources to the euphotic zone.

From September 1997 until December 2010, a near-continuous record of global satellite ocean color observations was available from the Sea viewing Wide-Field of view Sensor (SeaWiFS) mission (e.g., McClain et al. 2004; McClain 2009). Great efforts were made to insure the stability and accuracy of the SeaWiFS radiometric calibration, enabling investigators to address relationships among ocean environmental conditions and phytoplankton productivity (e.g., Behrenfeld et al. 2006; McClain 2009; Siegel et al. 2012, manuscript submitted to *Remote Sens. Environ.*). The ecosystem property most often derived from ocean color data is surface chlorophyll concentration (Chl). Chl provides a measure of phytoplankton pigments and its variability reflects the combined influences of changes in phytoplankton biomass and its physiological responses to light and nutrient levels (e.g., Falkowski 1984; Behrenfeld et al. 2005, 2008; Siegel et al. 2005; Siegel et al. 2012, manuscript submitted to *Remote Sens. Environ.*). Figure 3.36 shows the SeaWiFS mission (November 1997–November 2010) mean fields of Chl. Values of Chl span three orders of magnitude globally (0.03 mg m^{-3} to > 30 mg m^{-3}) and their spatial patterns mimic large scale climatological patterns in Ekman pump-

ing and seasonal convective mixing (Sverdrup 1955; Yoder et al. 1993). Higher values of Chl are found in regions of seasonal deep mixing (e.g., North Atlantic and Southern Oceans) and sustained vertical upwelling (e.g., equatorial Atlantic and Pacific Oceans, off California and Peru coasts), while low values are found in the low-nutrient, permanently stratified central ocean gyres (Fig. 3.36).

Unfortunately, the SeaWiFS ceased operating in December 2010 and assessments of global ocean phytoplankton for 2011 require other satellite data assets. Here, observations from NASA's Moderate Resolution Imaging Spectroradiometer (MODIS) on the Aqua platform and the European Space Agency's (ESA) Medium-Resolution Imaging Spectrometer (MERIS) instruments[1] are used. Observations of chlorophyll concentration, using bio-optical algorithms similar to the SeaWiFS operational algorithms, were available from both sensor datasets and monthly binned imagery starting in July 2002 for both MODIS and MERIS. Raw data from the two satellite sensors are collected and processed by different groups, although many of the same field data and algorithms are employed for both (processing details are in the references listed in the caption for Fig. 3.37). Consequentially, the methods and source data used to track temporal changes in the satellite calibrations are different for MODIS and MERIS (e.g., NRC 2011).

Anomalies of $\log_e$(Chl) for the year 2011 for both MODIS and MERIS are shown in Figs. 3.37a and b, respectively. Annual anomalies were calculated from monthly anomalies for each dataset summed over the year 2011. Natural log transformations are commonly used to interpret data that vary over many orders of magnitude and $\log_e$(Chl) anomalies can be interpreted as the difference in Chl normalized by its mean value, or simply a percentage change (Campbell 1995).

Both MODIS and MERIS chlorophyll values in 2011 show differences from the long-term mean that are greater than 40% in many areas (Figs. 3.37a,b). A good correspondence is found in the spatial locations of anomalous Chl values between the two datasets, although the MODIS Chl anomalies appear to be more negative overall. Both datasets find high values of Chl for 2011 throughout much of the tropical Pacific Ocean, subtropical North Atlantic Ocean, tropical Indian Ocean, and in portions of the Southern Ocean. Conspicuously low values of Chl during 2011 were found in the western Indian Ocean, the tropical Atlantic, and globally throughout the subtropics.

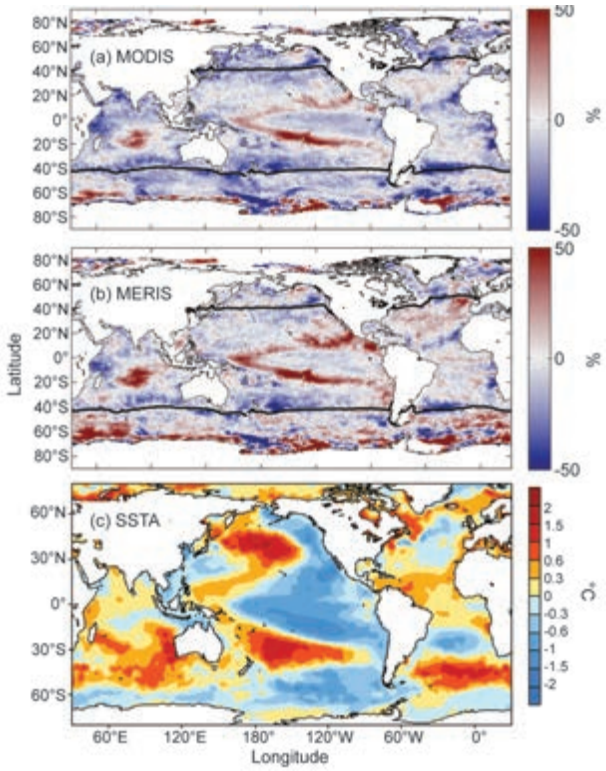

Fig. 3.37. Spatial distribution of summed monthly anomalies for 2011 for (a) MODIS $\log_e$(Chl) (% difference from climatology), (b) MERIS $\log_e$(Chl) (% difference from climatology), and (c) SST (°C). Anomalies are calculated on a 1° basis as differences in the year 2011 from monthly mean distribution over available data from each mission. MODIS observations are from Reprocessing 2010.0 (http://oceancolor.gsfc.nasa.gov/WIKI/OCReproc20100MA.html). MERIS observations are from its third data processing (http://earth.eo.esa.int/pcs/envisat/meris/documentation/meris_3rd_reproc/MERIS_3rd_Reprocessing_Changes.pdf). SST anomalies are based upon the Reynolds weekly SST version 2.

The climate state of 2011 can be characterized by the development of a strong La Niña event during the second half of the year and a strong negative Pacific decadal oscillation (PDO; see section 3b). In fact, the "wishbone" shaped feature indicative of a La Niña transition can be seen in the log-transformed Chl distribution across the tropical Pacific (Figs. 3.37a,b). The 2011 SST anomaly (SSTA; Fig. 3.37c) is indicative of a reemergence of La Niña conditions, strengthening of negative PDO, development of a positive Indian Ocean dipole, and above-normal SST values in the tropical North Atlantic and midlatitude Southern

1 Note communication with the Envisat satellite (which hosts MERIS) ceased on April 8, 2012. This will likely end the MERIS satellite ocean color record presented here (see http://www.esa.int/esaCP/SEMQ2EHWP0H_index_0.html for further details).

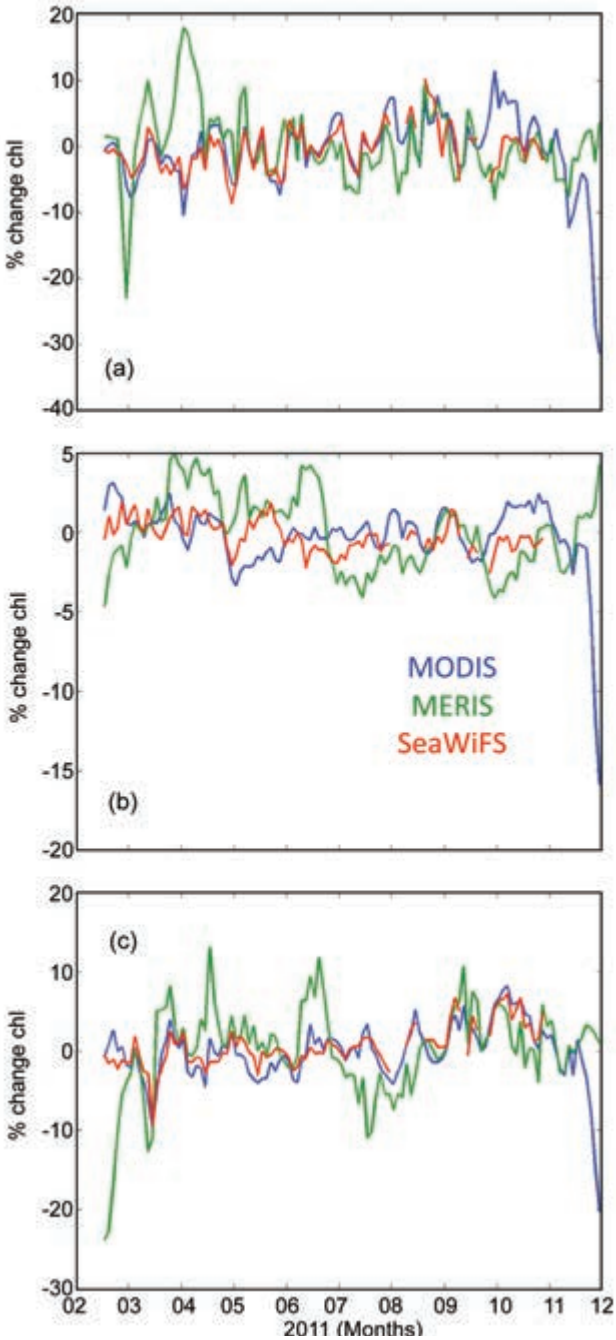

Fig. 3.38. Monthly anomalies for $\log_e$(Chl) averaged over (a) the cool region of the Northern Hemisphere oceans (mean SST < 15°C), (b) the warm ocean (mean SST > 15°C), and (c) the cool region of the Southern Hemisphere oceans for the SeaWiFS (red), MODIS (blue), and MERIS (green) data records. Figure 3.36 shows the location of the mean 15°C isotherm. Values are calculated from 1° gridded monthly log-transformed anomalies using each mission's climatology following procedures from previous State of the Climate reports and other publications (e.g., Behrenfeld et al. 2006; 2009; O'Malley et al. 2010; Siegel et al. 2011).

Oceans (see section 3b). These patterns in SSTA imprint generally inverse signals in the Chl anomalies (compare Figs. 3.37a,b with Fig. 3.37c). However, the expected inverse relationship is not perfect and high/low Chl anomalies are found where the SSTA signals are mixed, such as in the tropical Indian Ocean.

To place the year 2011 in a broader climatological context monthly anomalies of $\log_e$(Chl) averaged over the cool region of the Northern Hemisphere (NH) oceans (Fig. 3.38a, mean SST < 15°C), the warm ocean (Fig. 3.38b, mean SST > 15°C), and the cool region of the Southern Hemisphere (SH) oceans (Fig. 3.38c) for the SeaWiFS (red), MODIS (blue) and MERIS (green) data records are compared. (The black line in Fig. 3.36 shows the location of the mean 15°C isotherm.) Anomalies are calculated as the difference in monthly log-transformed chlorophyll determinations for each 1° bin from the respective mission's climatology and then summed over the three regions of interest. As before, the natural log-transformed anomalies can be interpreted as percent differences from normal conditions. This evaluation of long-term temporal anomalies follows procedures from previous *State of the Climate* reports and other publications (e.g., Behrenfeld et al. 2006, 2009; O'Malley et al. 2010; Siegel et al. 2012, manuscript submitted to *Remote Sens. Environ.*).

For the most part, aggregate Chl anomalies are bounded approximately by ±10% differences from normal conditions for the cool oceans (Figs. 3.38a,c) and roughly ±4% for the warm oceans (Fig. 3.38b). Conspicuous outliers are found for the MERIS mission early in the record (particularly for the cool ocean aggregates) and for the MODIS record in late 2011. Sampling is likely to have an important role in the dispersion of results for the high latitude aggregates during the winter because high solar zenith angles greatly reduce the extent of the regions where good ocean color assessments can be made. The MODIS record for the last part of 2011 is 15% to about 30% lower than normal conditions, depending on the ocean region. This extreme result is neither expected nor supported by the MERIS data record, which instead shows positive Chl anomalies in late 2011 for the warm ocean (Fig. 3.38b).

The disparity among satellite data records illustrated in Fig. 3.36, especially for 2011, clearly challenges the ability to distinguish global ocean ecosystem changes over interannual time scales. While the global aggregate time series (Fig. 3.38) shows only a fair correspondence between missions, the spatial patterns for 2011 anomalies look broadly similar for

MODIS and MERIS (Figs. 3.37a,b). The calculation of the global aggregates averages over many regional-scale anomaly features, creating a time series where smaller, persistent biases become apparent. This means that details in satellite sensor performance, data processing, and tracing of radiometric standards are very important when global aggregates are created and long-term trends are interpreted (e.g., Antoine et al. 2005; Siegel and Franz 2010; NRC 2011; Siegel et al. 2012, manuscript submitted to *Remote Sens. Environ.*).

The SeaWiFS data record made extensive use of external standards (lunar views and intense ground efforts) to monitor changes in sensor gains and offsets over time and to set the sensor's absolute calibration (e.g., Franz et al. 2007; McClain 2009). The relative uncertainty levels in lunar calibrations for SeaWiFS's top of the atmosphere reflectance determinations were ~0.1% (compared with the low-frequency fit relationship), making SeaWiFS the long-term standard against which other satellite ocean color records are compared (e.g., Franz et al. 2007; Eplee et al. 2011; NRC 2011; Siegel et al. 2012, manuscript submitted to *Remote Sens. Environ.*). The recent *Sustained Ocean Color Observations* report (NRC 2011) made important recommendations based on lessons learned from previous ocean color missions such as SeaWiFS. Several recommendations from the report highlighted the importance of assessing changes in radiometric calibration over time and the repeated reprocessing of these data streams (NRC 2011).

Neither MODIS nor MERIS were designed to make monthly lunar views through the Earth viewing telescope that illuminates the complete optical path and all radiometric detectors (as SeaWiFS does). Consequently, other means have been employed to trace changes in sensor calibration over time (summarized in NRC 2011). Briefly, MERIS relies on a dual solar diffuser approach where changes in the primary diffuser are monitored by a second diffuser that is infrequently exposed to sunlight (Rast and Bezy 1999; Delwart and Bourg 2011). The tracking of radiometric changes in MERIS is further complicated by the sensor design, which employs multiple cameras with multiple detectors per camera to span the cross-track view. Similarly, MODIS temporal calibration is complicated by the scanner design, which relies on a rotating scan mirror (rather than a rotating telescope) for cross-track observation and leads to different temporal changes at each scan angle. MODIS requires both a solar diffuser calibration and lunar observations to track changes in radiometric calibration (Xiong et al. 2010). However, these on-board measurements are insufficient to fully characterize the changes at all scan angles or to assess changes in polarization sensitivity (Franz et al. 2008) and additional calibration sources have been used to augment the on-board calibration system (Kwiatkowska et al. 2008; Meister et al. 2012). The MODIS Aqua dataset presented here (version 2010.0) used SeaWiFS as a calibration source when it was available (Meister et al. 2012). The severe underestimates of Chl levels for 2011 shown in Fig. 3.38 are caused to large degree by the lack of SeaWiFS observations to cross-calibrate the MODIS sensor signals. Work is currently underway to use natural ground (land) targets to correct the MODIS Aqua signals in the absence of SeaWiFS observations (B. Franz 2012, personal communication). These are details, but the details are critical for assessing long-term changes in satellite ocean color observations—particularly at global scales.

The ecology and biogeochemistry of the oceans are constantly changing in response to climate variability and change. These changes of the ocean biosphere exhibit tremendous spatial heterogeneity that cannot be sampled adequately from point-source or ship-based measurements. Viewing integrated global ocean responses is the province of satellite observations and, for the moment, the ability to visualize these changes is impaired. Regaining full vision will require creative approaches for characterizing current space assets, continually reevaluating and reprocessing existing datasets, and focusing priorities of future sensors on the end-to-end mission requirements that ensure the retrieval of global, climate-quality data products over the lifetime of ocean sensor missions.

Libraries: Please file with the *Bulletin of the American Meteorological Society*, Vol. 93, Issue 7